Momentum distribution of the uniform electron gas at finite temperature: Effects of spin polarization

Tobias Dornheim,[1,2,*] Jan Vorberger,[2] Burkhard Militzer,[3,4] and Zhandos A. Moldabekov[1,2]

[1]*Center for Advanced Systems Understanding (CASUS), D-02826 Görlitz, Germany*

[2]*Helmholtz-Zentrum Dresden-Rossendorf (HZDR), D-01328 Dresden, Germany*

[3]*Department of Earth and Planetary Science, University of California, Berkeley, California 94720, USA*

[4]*Department of Astronomy, University of California, Berkeley, California 94720, USA*

(Received 3 June 2021; accepted 25 October 2021; published 22 November 2021)

We carry out extensive direct path integral Monte Carlo (PIMC) simulations of the uniform electron gas (UEG) at finite temperature for different values of the spin-polarization ξ. This allows us to unambiguously quantify the impact of spin effects on the momentum distribution function $n(\mathbf{k})$ and related properties. We find that interesting physical effects like the interaction-induced increase in the occupation of the zero-momentum state $n(\mathbf{0})$ substantially depend on ξ. Our results further advance the current understanding of the UEG as a fundamental model system, and are of practical relevance for the description of transport properties of warm dense matter in an external magnetic field. All PIMC results are freely available online and can be used as a benchmark for the development of methods and applications.

DOI: 10.1103/PhysRevE.104.055206

I. INTRODUCTION

The uniform electron gas (UEG) [1,2] is one of the most fundamental model systems in theoretical physics and related disciplines. In particular, the UEG has been pivotal for the development of groundbreaking concepts such as Fermi liquid theory [2], the Bardeen-Cooper-Schrieffer theory of superconductivity [3], and the quasiparticle picture of collective excitations [4]. Despite its apparent simplicity, it exhibits a wealth of interesting physical effects such as Wigner crystallization [5,6], a potentially incipient excitonic mode at low density [7–9], and the possibility of a charge-density or spin-density wave [2,10,11]. Consequently, the accurate description of the UEG based on ground-state quantum Monte Carlo (QMC) simulations [12,13] has been important for many applications such as the emergence of density-functional theory [14].

Over the last decades, there has emerged growing interest in so-called *warm dense matter* (WDM), an exotic state characterized by extreme temperatures and densities [15,16]. In nature, these conditions occur in astrophysical objects such as giant-planet interiors [16–19], brown dwarfs [20,21], and neutron star crusts [22]. Furthermore, WDM plays an important role in cutting-edge technological applications such as inertial confinement fusion [23], hot-electron chemistry [24], and the discovery of materials [25–27]. From a theory point of view, WDM is defined by two characteristic parameters that are simultaneously of the order of unity: (1) the density parameter (also known as the Wigner-Seitz radius or quantum coupling parameter [28]) $r_s = \bar{r}/a_\mathrm{B}$, with $\bar{r}$ and a_B being the average interparticle distance and first Bohr radius, and (2) the reduced temperature $\theta = k_\mathrm{B}T/E_\mathrm{F}$, with E_F being the usual Fermi energy, cf. Eq. (12).

Phenomenologically, these conditions manifest as the highly nontrivial interplay of quantum effects, Coulomb coupling, and thermal excitations, which renders WDM theory a most formidable challenge [29,30]. Coming back to the UEG, it has become clear that previous ground-state descriptions of the UEG are often not sufficient for applications in the WDM regime [31–33]. Consequently, a gamut of theoretical methods has been introduced to describe electrons at these conditions. A particularly successful approach are dielectric theories [34,35], which have been adapted to finite temperature mainly in the works by Tanaka and Ichimaru and Ichimaru *et al.* [36,37] in the 1980s and are continually being developed [10,38–42] and used for various practical applications [43,44]. Other prominent examples include diagrammatic techniques [45–47], quantum-to-classical mapping schemes [48–51], and nonequilibrium Green's functions [52,53]. While all of the aforementioned methods have substantially improved our understanding of electrons in the WDM regime, they are afflicted with systematic errors such that the accuracy of these data has remained unclear.

This unsatisfactory situation has sparked a surge of developments in the field of fermionic QMC simulations at finite temperatures [54–65] (see Ref. [66] for a review), which has culminated in the first accurate parametrizations of the exchange-correlation free energy of the UEG at WDM conditions [67–70]. In particular, this allows for thermal density functional theory simulations on the level of the local density approximation [31,32], and constitutes the basis for the development of more sophisticated functionals that explicitly take into account the temperature [71,72]. Further progress on the UEG at WDM conditions includes the characterization of linear-response properties such as the static local field

*t.dornheim@hzdr.de

correction [73–76], numerical and theoretical results for the nonlinear electronic density response [77,78], and even the study of dynamic quantities based on the analytic continuation of imaginary-time correlation functions [9,73,79–81].

Another fundamental property of the UEG is the momentum distribution function $n(\mathbf{k})$, which can be directly accessed in experiments with positron annihilation spectroscopy in metals [82,83], and which is highly important for the development of accurate models for the computation of different transport properties of WDM [84]. At finite temperatures, the first QMC results have been presented by Militzer *et al.* [85,86] based on approximate restricted path integral Monte Carlo (PIMC) simulations. More recently, the momentum distribution of the unpolarized UEG has been revisited by Hunger *et al.* [87], who have carried out exact configuration PIMC simulations at high densities ($r_s \lesssim 1$), and by Dornheim *et al.* [88] on the basis of exact direct PIMC simulations going from metallic densities $r_s \sim 2$ to the strongly coupled electron liquid regime ($r_s \sim 10 - 100$). More specifically, these studies have addressed interesting phenomena such as the interaction-induced increase in the occupation of the zero-momentum state [47,85], the related negative exchange-correlation part to the kinetic energy K_{xc}, and the algebraic tail in the limit of large momenta k, cf. Eq. (14) below.

At the same time, a thorough investigation of the dependence of the momentum distribution function on the spin polarization $\xi = (N^{\uparrow} - N^{\downarrow})/N$ (with $N^{\uparrow}$, $N^{\downarrow}$, and N being the number of spin-up electrons, spin-down electrons, and all electrons, respectively) has yet been missing. In the present paper, we aim to fill this gap by presenting extensive direct PIMC results for $n(\mathbf{k})$ for different values of ξ. First, we mention that such an investigation is interesting in its own right, and helps to significantly advance our current understanding of the UEG as a fundamental model system [69,70]. Second, the impact of the spin polarization is of central importance for the properties of WDM in an external magnetic field. In the case of strong electronic degeneracy ($\theta \ll 1$) in a nonquantizing magnetic field, the effect of the spin polarization on transport properties is negligible as it scales as $\xi \sim \mathcal{O}(\theta)$ [89]. Similarly, quantum effects are not relevant due to strong thermal excitations in the regime of very high temperatures, $\theta \gg 1$. In stark contrast, the effects of the spin polarization play an important role precisely in the WDM regime ($\theta \sim 1$) in an external magnetic field, as both aforementioned conditions do not apply here. More specifically, the condition for a nonquantizing magnetic field follows from the requirement that the electron cyclotron energy $\hbar\omega_c$ is much smaller than the characteristic quantum kinetic energy $\sqrt{E_F^2 + T^2}$ [90]. From this condition, one can find that the range of nonquantizing magnetic fields is given by $B/B_0 \ll \frac{18.4}{r_s^2}\sqrt{\theta^2 + 1}$ (where $B_0 \simeq 2.25 \times 10^5$T). For example, at $\theta \sim 1$ and $r_s \sim 1$, nonquantizing strong magnetic fields $B \sim 10$ T $- 10^4$ T can be generated in experiments related to inertial confinement fusion [91,92]. Yet, the physical properties of WDM in such strong magnetic fields remain largely unknown. We are thus convinced that our results for the impact of the spin polarization on the momentum distribution are of direct importance for the future exploration of WDM at these extreme conditions.

Furthermore, we mention that, in addition to its relevance for the field of WDM, the UEG at finite T can be approximately realized in semiconductors [2,93], which can be tuned experimentally to a high degree. Finally, we note that the employed direct PIMC method constitutes the method of choice for the present paper, as it is capable of giving exact results that can be used as a benchmark for other approaches like restricted PIMC. At the same time, we stress that other methods are superior for other parameters, such as high densities ($r_s \lesssim 0.1$), when relativistic effects become dominant.

The paper is organized as follows: In Sec. II, we introduce the required theoretical background including the PIMC method (Sec. II A), the corresponding estimation of the momentum distribution function (Sec. II B), and the spin-resolved reduced system parameters (Sec. II C). Section III is devoted to the presentation of our simulation results, starting with PIMC data for the fully spin-polarized case (Sec. III A). Subsequently, we extend these considerations to arbitrary values of the spin polarization in Sec. III B. The paper is concluded by a brief summary and discussion in Sec. IV.

II. THEORY

We assume Hartree atomic units throughout this paper.

A. The path integral Monte Carlo method

Throughout this paper, we simulate $N = N^{\uparrow} + N^{\downarrow}$ spin-restricted electrons in a cubic simulation box of constant volume $V = L^3$, and at a fixed temperature $T = 1/\beta$. Further, we restrict ourselves to the case of thermodynamic equilibrium, and the expectation value of a physical observable $\hat{O}$ is given by

$$\langle \hat{O} \rangle = \frac{1}{Z} \text{Tr}\big(\hat{\rho}\hat{O}\big). \tag{1}$$

Here $\hat{\rho} = \exp(-\beta\hat{H})$ denotes the (unnormalized) canonical density operator and the normalization is given by the corresponding canonical partition function Z. The basic idea of the PIMC method [94–96] is the stochastic evaluation of the matrix elements of $\hat{\rho}$. More specifically, this requires the evaluation of extremely high-dimensional integrals, which is accomplished efficiently using variations of the Metropolis Monte Carlo method [97]. While being computationally involved, the PIMC method is, in principle, capable of providing a quasiexact solution of the quantum N-body problem of interest. The term *quasiexact* implies that PIMC estimations of Eq. (1) can be made arbitrarily accurate in a controlled way when the convergence parameters (typically the number of imaginary-time slices P and the number of Monte Carlo samples N_{MC}) are increased. A more detailed introduction to the PIMC method is beyond the scope of the current paper, and the interested reader is referred to Refs. [69,94,98].

An additional problem arises due to the fermionic nature of electrons, which manifests as an antisymmetry under the exchange of particle coordinates in Eq. (1). This is the origin of the notorious fermion sign problem [99–101], which leads to an exponential increase in computation time with increasing the system size N or decreasing the temperature T; see Refs. [101,102] for an accessible topical discussion. A

popular approach to circumvent this issue is the application of the fixed-node approximation [103] (commonly known as *restricted* PIMC or RPIMC), which formally removes the sign problem for simulations in the canonical ensemble. Indeed, the RPIMC method constitutes at present the only QMC approach that is capable of simulating real materials in the WDM regime, e.g., Refs. [104–106]. Unfortunately, this great advantage comes at the cost of an uncontrolled approximation, as the exact nodes of correlated quantum many-body systems are *a priori* unknown. More specifically, Schoof *et al.* [56] have shown that RPIMC leads to errors of up to 10% in the description of exchange–correlation properties of electrons in the WDM regime.

For this reason, we do not impose any nodal restriction in the present paper. Consequently, our *direct* PIMC simulations are computationally extremely demanding, and we spend up to $\mathcal{O}(10^5)$ CPUh for a single density-temperature combination in the most challenging regime. Still, the sign problem constitutes the main limitation of our approach and prevents us from accessing the low-temperature regime ($\theta < 1$) except for very strong coupling.

B. PIMC estimation of the momentum distribution

The momentum distribution of N_σ (with $\sigma \in [\uparrow, \downarrow]$ denoting the spin) electrons is defined as [86]

$$n_\sigma(\mathbf{k}) = \frac{(2\pi)^d}{V}\left\langle \sum_{l=1}^{N_\sigma} \delta(\hat{\mathbf{k}}_l - \mathbf{k}) \right\rangle, \tag{2}$$

with the corresponding normalization

$$\sum_{\mathbf{k}} n_\sigma(\mathbf{k}) = N_\sigma. \tag{3}$$

In addition, we mention that Eq. (2) is related to the off-diagonal density matrix in coordinate space $n_\sigma(s) \coloneqq n_\sigma(\mathbf{r}, \mathbf{r}')$, with $s = |\mathbf{r} - \mathbf{r}'|$, by

$$n_\sigma(\mathbf{k}) = \int \mathrm{d}\mathbf{s}\, n_\sigma(\mathbf{s}) e^{-i\mathbf{s}\cdot\mathbf{k}}. \tag{4}$$

For an ideal (i.e., noninteracting) Fermi system, Eq. (2) is given by the well-known Fermi distribution

$$n_0(\mathbf{k}) = \frac{1}{1 + \exp[\beta(E_\mathbf{k} - \mu)]}, \tag{5}$$

with μ being the usual chemical potential [2], and the ideal dispersion relation

$$E_\mathbf{k} = \frac{\mathbf{k}^2}{2}. \tag{6}$$

Interestingly, the evaluation of Eq. (2) is not straightforward in the PIMC method, as it constitutes an off-diagonal observable in the underlying coordinate representation. More specifically, each particle is represented as a closed path over different coordinates in the imaginary time within the PIMC method. In contrast, the estimation of $n(\mathbf{k})$ requires the presence of a single *open* path within the PIMC simulation, thereby resulting in a modified configuration space. This is illustrated in Fig. 1 for a schematic configuration of $N = 3$ electrons on $P = 6$ imaginary-time slices (with $\epsilon = \beta/P$ being a discretized time step), depicted in the τ-x plane. While

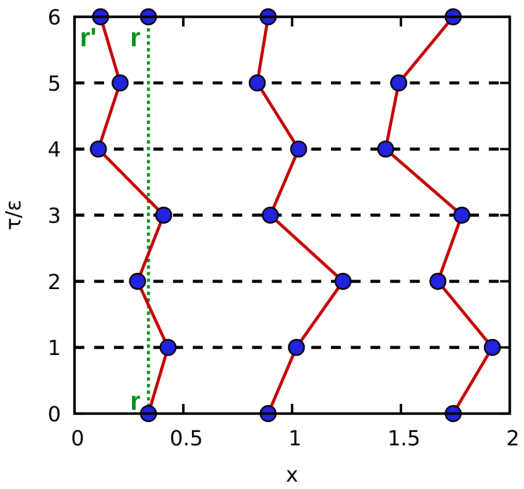

FIG. 1. Schematic illustration of the off-diagonal configuration space $Z_{\mathbf{r},\mathbf{r}';\sigma}$ including a single open trajectory with different start and end points $\mathbf{r}$ and $\mathbf{r}'$. Adapted from Ref. [88] with the permission of the authors.

the two rightmost paths exhibit the same coordinates for $\tau = 0$ and $\tau = \beta$, the electronic path on the left is *open* and has different coordinates $\mathbf{r}$ and $\mathbf{r}'$ at its start and end.

The expression for Eq. (2) in the path-integral picture is then given by [86,94]

$$n_\sigma(\mathbf{k}) = \frac{1}{V}\frac{Z_{\mathbf{r},\mathbf{r}';\sigma}}{Z}\langle e^{i\mathbf{k}(\mathbf{r}-\mathbf{r}')}\rangle_{\mathbf{r},\mathbf{r}';\sigma}, \tag{7}$$

where the subscript of the angular brackets indicates this modified configuration space, and $Z_{\mathbf{r},\mathbf{r}';\sigma}$ its corresponding normalization. In practice, we use the extended-ensemble approach presented in Ref. [88], which is based on the worm algorithm by Boninsegni *et al.* [98,107]. One particular strength of this scheme compared to earlier works [86,94] is the possibility to directly compute the normalization of Eq. (7) without the need for a subsequent fitting of the off-diagonal density matrix $n(\mathbf{r}, \mathbf{r}')$ or an artificial imposition of the condition in Eq. (3). The practical implications of this advantage are discussed in Sec. III A below.

C. Reduced system parameters for arbitrary spin-polarizations

To understand the effect of an arbitrary spin-polarization $\xi \in [0, 1]$ on physical observables, it is helpful to consider modified, explicitly spin-resolved reduced parameters. To this end, we introduce the spin-resolved density parameter r_s^σ via the relation

$$\frac{4}{3}\pi\left(r_s^\sigma\right)^3 = \frac{V}{N^\sigma}, \tag{8}$$

which immediately gives

$$r_s^\sigma = r_s\left(\frac{N}{N^\sigma}\right)^{1/3}. \tag{9}$$

Furthermore, Eq. (9) can be expressed in terms of the spin polarization ξ as

$$r_s^\uparrow = r_s\left(\frac{1+\xi}{2}\right)^{-1/3} \text{ and} \tag{10}$$

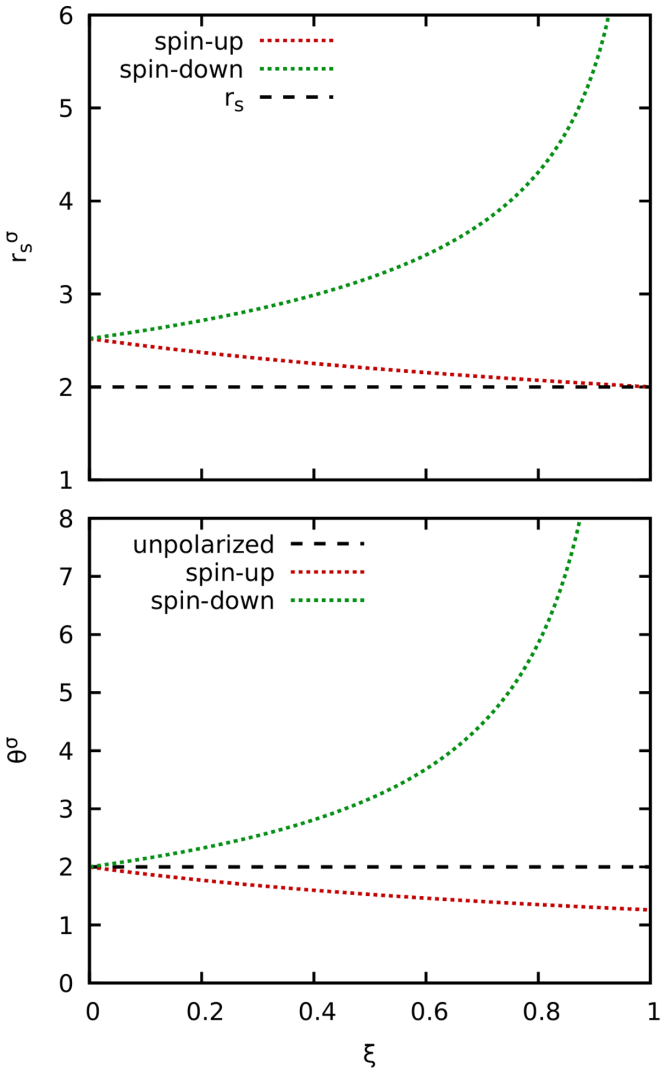

FIG. 2. Polarization dependence of the spin-resolved density parameter r_s^σ (top panel) and reduced temperature θ^σ (bottom panel) for $r_s = 2$ and $\theta = 2$ (using the Fermi energy of the unpolarized system as a reference).

$$r_s^\downarrow = r_s \left(\frac{1-\xi}{2} \right)^{-1/3}.$$

The dependence of Eqs. (10) on ξ is shown in the top panel of Fig. 2, using a total density parameter $r_s = 2$ as a reference (dashed black line). For $\xi = 0$, the system is fully unpolarized, i.e., $N^\uparrow = N^\downarrow = N/2$, which immediately gives $r_s^\uparrow = r_s^\downarrow = 2^{1/3} r_s$. Upon increasing ξ, the fraction of spin-up electrons increases, and, consequently, $r_s^\uparrow$ converges towards the full density parameter r_s in the limit of $\xi = 1$. In contrast, the number density of spin-down electrons decreases with ξ and eventually attains zero. Thus, $r_s^\downarrow$ actually diverges towards the fully spin-polarized case.

A second parameter that is relevant to the present paper is given by the spin-resolved reduced temperature, which we simply express as a function of r_s^σ,

$$\theta^\sigma(\beta) = \frac{1}{\beta E_\mathrm{F}^\sigma \left(r_s^\sigma \right)}, \tag{11}$$

with $E_\mathrm{F}^\sigma(r_s^\sigma)$ being the Fermi energy for a fully spin-polarized system with the density parameter r_s^σ,

$$E_\mathrm{F}^\sigma(r_s^\sigma) = \frac{\left(\mathbf{k}_\mathrm{F}^\sigma\right)^2}{2}, \tag{12}$$

with the corresponding spin-dependent Fermi wave number:

$$k_\mathrm{F}^\sigma = (6\pi^2 n^\sigma)^{1/3}. \tag{13}$$

The results for Eq. (11) are shown in the bottom panel of Fig. 2, using $\theta = 2$ as a reference for the unpolarized case. With increasing ξ, the number density of the spin-up electrons is increased, which results in a larger Fermi energy. Therefore, the reduced temperature is decreased when β (or, equivalently, T) are being kept constant. Conversely, both the number density of the spin-down electrons and the corresponding Fermi energy vanish toward $\xi = 1$, which means that $\theta^\downarrow$ diverges.

III. RESULTS

A. The spin-polarized electron gas

1. Density dependence

Let us start our investigation of spin effects on the momentum distribution with an analysis of the fully spin-polarized case, $\xi = 1$. To this end, we show the density dependence of $n(\mathbf{k})$ for $\theta^\uparrow = 1$ in Fig. 3. More specifically, the dashed black curve shows results for the ideal Fermi gas [cf. Eq. (5)], which are independent of the density when the reduced temperature is being kept constant. In addition, the different symbols show our PIMC results that have been obtained for $N^\uparrow = 33$ electrons for different values of r_s. For completeness, we mention that the left and right panels correspond to a linear and logarithmic scale, which allows to focus on different features of $n(\mathbf{k})$ at different k. Furthermore, an extensive analysis of finite-size effects for different densities is shown in Sec. III B 1 below.

First and foremost, we find that all depicted data sets are qualitatively quite similar to the ideal Fermi distribution, which is substantially broadened at these conditions due to the comparably large thermal energy. For completeness, we mention that the PIMC data for $n(\mathbf{k})$ have been obtained within the canonical ensemble, whereas Eq. (5) is derived for the grand-canonical ensemble [2]. Still, this does not pose an inconsistency, as it is well-known that the different thermodynamic ensembles converge toward each other in the thermodynamic limit and finite-size effects in the PIMC data are shown to be small in Sec. III B 1 below.

Interestingly, the momentum distribution at zero momentum, $n(0)$, is increased compared to $n_0(0)$ for $r_s = 2$ (red circles), $r_s = 4$ (green crosses), and $r_s = 6$ (blue diamonds), and this trend even increases with r_s for these three cases. This fairly counterintuitive phenomenon was first reported by Militzer and Pollock [85], and can be explained in terms of a negative mean-field contribution to the single-particle dispersion. A more systematic investigation of this trend and its relation to the kinetic energy is shown in Fig. 4 below. For $r_s = 40$ (yellow triangles), the system becomes strongly correlated and we find $n(0) < n_0(0)$, although both are comparable in magnitude.

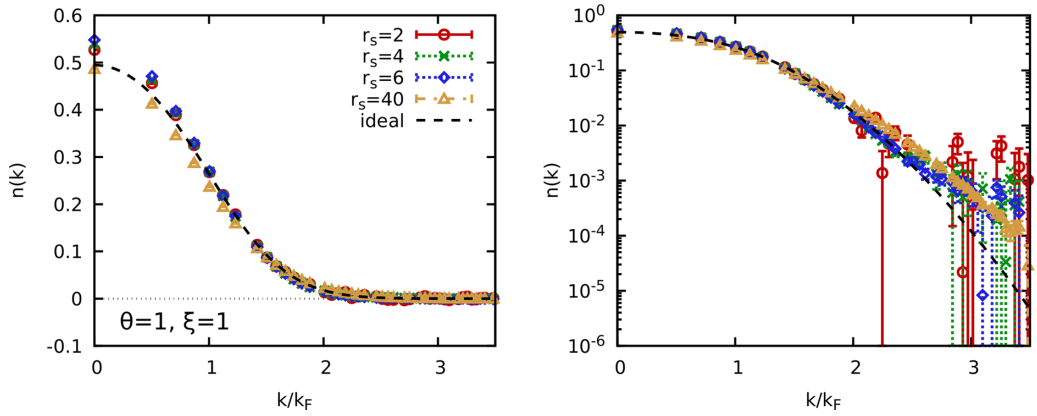

FIG. 3. Momentum distribution of the spin-polarized ($\xi = 1$) electron gas for $\theta^{\uparrow} = 1$. The dashed black curve shows results for the ideal Fermi gas [Eq. (5)], and the data points correspond to our PIMC data for different r_s. The left and right panels shows $n(\mathbf{k})$ on a linear and logarithmic scale, respectively.

The logarithmic depiction of $n(\mathbf{k})$ shown in the right panel of Fig. 3 allows us to study the behavior of the momentum distribution at large momenta, where it rapidly decays. Consequently, this regime is hard to resolve with the PIMC method and the relative noise level increases and eventually surpasses 100%. For the unpolarized UEG, it can be shown analytically that $n(\mathbf{k})$ decays algebraically in the limit of large k, and the exact relation is given by [108,109]

$$\lim_{k\to\infty} n(k) = \frac{4}{9}\left(\frac{4}{9\pi}\right)^{2/3}\left(\frac{r_s}{\pi}\right)^2 \frac{k_F^8}{k^8} g^{\uparrow\downarrow}(0), \tag{14}$$

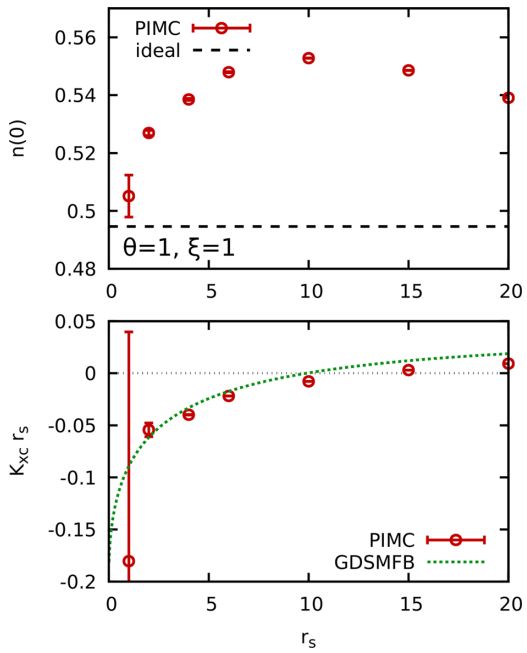

FIG. 4. Top: r_s dependence of $n(0)$ for the spin-polarized UEG with $\theta^{\uparrow} = 1$. Bottom: r_s dependence of the exchange–correlation part to the kinetic energy (per particle) K_{xc} [Eq. (16)], with the red circles being our PIMC results and the dotted green line having been computed from Eq. (17) using the parametrization by Groth *et al.* [68].

with $g^{\uparrow\downarrow}(0)$ being the pair correlation function between electrons of opposite spin, which has been parametrized in Ref. [75] for different values of r_s and θ. This relation has recently been verified on the basis of highly accurate numerical data by Hunger *et al.* [87]. For the spin-polarized case, on the other hand, Eq. (14) cannot hold as there is only a single spin component, and the on-top pair correlation function is always zero. Instead, Rajagopal *et al.* [110] have found the relation

$$\lim_{k\to\infty} n(k) = \frac{4}{3}\frac{8}{9\pi^2}(\alpha r_s)^2 \frac{g^{\uparrow\uparrow\prime\prime}(0)}{2}\left(\frac{k_F}{k}\right)^{10}, \tag{15}$$

with $\alpha = (\frac{4}{9\pi})^{1/3}$, which depends on the second derivative of the pair correlation function between electrons of equal spin, again at zero distance. While being asymptotically exact, Eqs. (14) and (15) do not give any information about the particular values of k for which these limits are attained in practice. The empirical findings for the unpolarized case in Ref. [87] indicate that this happens for $k \gtrsim 5k_{\mathrm{F}}$ at these conditions. Therefore, resolving the asymptotic tail would require us to accurately estimate the momentum distribution over at least eight orders of magnitude in $n(\mathbf{k})$ itself, which is beyond the capability of PIMC methods operating in coordinate space. The same issue has been reported by Dornheim *et al.* [88] for the unpolarized case, too.

Let us next get back to the topic of the counter-intuitive, interaction-induced increase of $n(0)$, which we analyze in detail in the top panel of Fig. 4. More specifically, the horizontal dashed black line corresponds to the ideal Fermi gas, which does not depend on r_s. In addition, the red circles show our PIMC data for different densities. First, we note the increasing error bars toward small r_s, which are a direct consequence of the fermion sign problem. More specifically, a decrease in the coupling strength leads to an increase in the frequency of permutation cycles within the PIMC simulation, and cycles of adjacent lengths contribute with a different sign. The resulting cancellation of positive and negative terms then leads to a decreasing signal-to-noise ratio; see Refs. [101,111] for more detailed information.

In the limit of $r_s \to 0$, the UEG becomes ideal [69] and the PIMC data approach the horizontal line. With increasing coupling strength, the occupation at $k = 0$ systematically in-

creases, and attains a maximum at $r_s \approx 10$ at these conditions. Increasing the density parameter even further leads to the opposite trend and, eventually, $n(0)$ will even become smaller than $n_0(0)$ as the electrons are pushed to larger k by the strong repulsion. The particular comparison between $n(\mathbf{k})$ and $n_0(\mathbf{k})$ strongly depends on the value of ξ, which is explained in detail below.

Let us next consider the connection between the correlation-induced increase in the momentum distribution at zero momentum to the exchange-correlation part of the kinetic energy,

$$K_{\rm xc} = K - E_0, \tag{16}$$

where K and E_0 are the total kinetic energy of the interacting and noninteracting system, respectively. For completeness, we mention that $K_{\rm xc}$ is directly related to the asymptotic behavior of the electronic local field correction at large wave numbers [74,112,113]. The r_s dependence of Eq. (16) is shown in the bottom panel of Fig. 4 for the same conditions as $n(0)$. More specifically, the red circles have been obtained by taking our direct PIMC results for K for $N = 33$ electrons and subsequently subtracting E_0 (taken from Ref. [60]) for the same system size. The large error bars for small r_s are again a direct consequence of the fermion sign problem, which is exacerbated by the definition of $K_{\rm xc}$ as the difference between two quantities that are more or less comparable in magnitude. Furthermore, the dotted green curve has been computed from the parametrization of the exchange-correlation free energy $f_{\rm xc}$ by Groth *et al.* [68] by evaluating the relation [69]

$$K_{\rm xc} = -f_{\rm xc}(r_s,\theta) - \theta \frac{\partial f_{\rm xc}(r_s,\theta)}{\partial \theta}\bigg|_{r_s} - r_s \frac{\partial f_{\rm xc}(r_s,\theta)}{\partial r_s}\bigg|_{\theta}. \tag{17}$$

First and foremost, we note the good qualitative agreement between Eq. (17) and the PIMC data, although there appear small but significant differences toward large r_s. The most likely explanation for the latter are finite-size effects in the red circles in either (or both) K or E_0, whereas the green curve has been constructed in the thermodynamic limit, i.e., in the limit of an infinite number of particles taken at a constant number density. A second, somewhat less likely explanation is the finite accuracy of the utilized parametrization of $f_{\rm xc}$, which might be exacerbated by the evaluation of the derivatives in Eq. (17).

From a physical perspective, we do indeed find a lowering in the kinetic energy due to electronic exchange-correlation effects for $r_s \lesssim 10$, whereas the total kinetic energy is increased for stronger coupling. Therefore, the negative values of $K_{\rm xc}$ are certainly related, but not equal to the increase in $n(0)$ discussed above, which is consistent with recent findings for the unpolarized electron gas [88].

2. Comparison to restricted PIMC

Let us conclude this study of the purely spin-polarized UEG with a comparison between our direct PIMC results for $n(\mathbf{k})$ and the restricted PIMC data by Militzer *et al.* [86]. This is shown in Fig. 5, where the top row corresponds to $r_s = 4$ and $\theta^\uparrow = 1$, i.e., a metallic density that is of relevance to contemporary WDM research [29]. The left panel shows results for $n(\mathbf{k})$ itself, and the ideal Fermi function (dashed black line) has been included as a reference. Further, the red circles and green crosses depict the PIMC and RPIMC data, respectively, which are in qualitative though not quantitative agreement. More specifically, the RPIMC data are systematically higher than the PIMC data, which is consistent to the recent findings by Dornheim *et al.* [88] for the unpolarized UEG. In the latter study, this discrepancy was explained by the normalization of $n(\mathbf{k})$, which is computed exactly within our extended ensemble formalism, but has to be inferred from the off-diagonal density matrix $n(\mathbf{r}, \mathbf{r}')$ in the case of RPIMC. Therefore, multiplying the RPIMC data by a constant factor of $Q = 0.977$ led to perfect agreement between direct PIMC and restricted PIMC for $\xi = 0$.

Following the same procedure (with the same factor) in the present case leads to the yellow crosses, which, indeed, are in excellent agreement to the PIMC data over the entire range of wave numbers. This can be seen particularly well in the right panel, where we show the relative deviation between the momentum distribution of the UEG and the ideal Fermi gas (in percent) with respect to $n_0(0)$,

$$\frac{\Delta n}{n(0)}[\%] = \frac{n(\mathbf{k}) - n_0(\mathbf{k})}{n_0(\mathbf{0})} \times 100. \tag{18}$$

In addition, this depiction also allows one to gain a more vivid insight into the behavior of $K_{\rm xc}$ shown in Fig. 4 above: For small momenta ($k \lesssim k_{\rm F}$), the momentum distribution function of the interacting electron gas plainly exceeds the ideal Fermi distribution $n_0(k)$, whereas the relative occupation is decreased in the range of $k_{\rm f} \lesssim k \lesssim 2k_{\rm F}$. Since the total kinetic energy is simply given by the integral

$$K = \frac{1}{2}\int {\rm d}\mathbf{k}\, n(\mathbf{k})\, \mathbf{k}^2, \tag{19}$$

the observed deviation profile directly indicates the relation $K[n(\mathbf{k})] < K[n_0(\mathbf{k})]$ at these conditions, thus resulting in the negative values of $K_{\rm xc}$ shown above.

We next consider the central row of Fig. 5, where we show the same analysis for $r_s = 40$ and $\theta^\uparrow = 1$. Physically, these conditions are located within the strongly coupled electron liquid regime [9,11], where the strong Coulomb repulsion between the electrons predominates over quantum degeneracy effects such as Pauli blocking or quantum diffraction. In particular, this regime is expected to give rise to a *negative dispersion relation* [9,73,80,81], which is of a potentially incipient excitonic nature [7,8]. At these conditions, the momentum distribution function of the interacting UEG compares markedly different to the ideal Fermi function, and the direct PIMC method predicts a depletion in the occupation at zero momentum, which holds for $k \lesssim 1.5k_{\rm F}$. While the raw RPIMC data (green crosses) actually predict an increase in $n(0)$ compared to the ideal system, this effect is most likely spurious. Specifically, multiplying the RPIMC data by the same factor Q as in the previous case leads to the yellow crosses, which, again, results in a perfect agreement to the direct PIMC data.

Let us conclude this comparison between the direct and restricted PIMC methods by investigating a lower temperature, $\theta^\uparrow = 0.5$, shown in the bottom row of Fig. 5. For completeness, we mention that such low values of the reduced

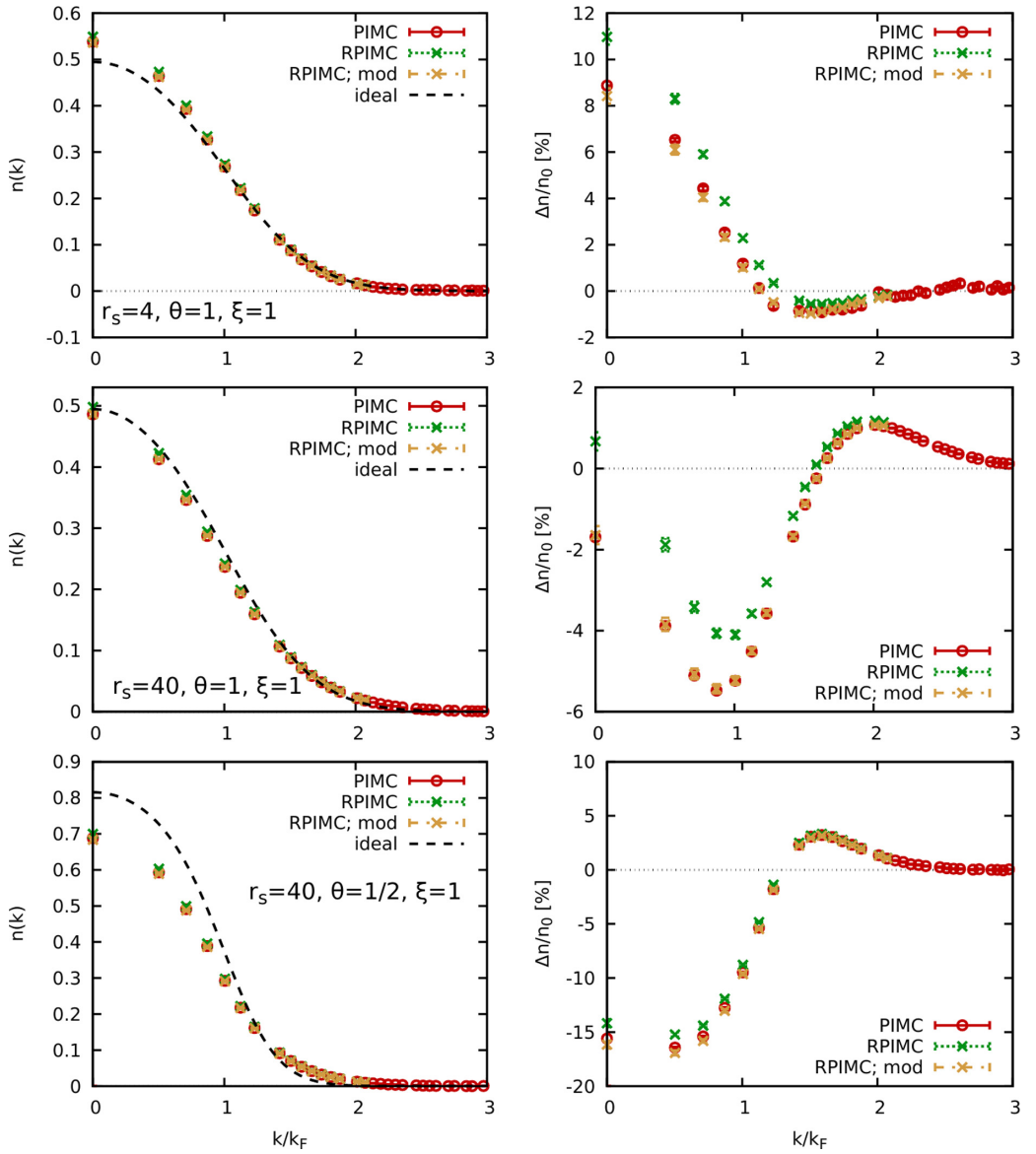

FIG. 5. Momentum distribution function of the spin-polarized ($\xi = 1$) UEG for $N = 33$ electrons. Top row: $r_s = 4$ and $\theta^{\xi=1} = 1$; center row: $r_s = 40$ and $\theta^{\xi=1} = 1$; bottom row: $r_s = 40$ and $\theta^{\xi=1} = 0.5$. Left column: $n(\mathbf{k})$, with the red circles, green crosses, and yellow crosses corresponding to our direct PIMC results, restricted PIMC results from Ref. [86], and modified RPIMC results (see text), respectively. Right column: Relative difference between $n(\mathbf{k})$ and $n_0(\mathbf{k})$ in percent, cf. Eq. (18).

temperature cannot be accessed by the direct PIMC method at metallic densities due to the aforementioned fermion sign problem. At these conditions, the occupation of momentum states at small k is substantially depleted compared to $n_0(k)$ as the electrons are pushed out to large momenta, resulting in a positive value of K_{xc}. The comparison between direct and restricted PIMC reveals the same issue with the normalization as in the two previous cases, and the thus modified yellow crosses agree with the red circles over the entire depicted k range.

In summary, the only systematic error that we can find in the RPIMC data both at $r_s = 4$ and $r_s = 40$ are due to the normalization and not a consequence of the fixed-node approximation that has been used to deal with the fermion sign problem. This is certainly encouraging, as the extended ensemble approach introduced in Ref. [88] can easily be incorporated into RPIMC as well, which would completely overcome this problem.

B. Intermediate polarizations and spin dependence

In the following section, we explicitly go beyond the purely ferromagnetic case to more closely isolate the effect of the spin polarization itself.

1. Analysis of finite-size effects

Being restricted to the description of a finite number of particles, PIMC results are in general afflicted with so-called finite-size effects [64,66,114–116]. Therefore, a careful analysis of the dependence of the results on the system size is usually indispensable. In the present paper, this is shown in

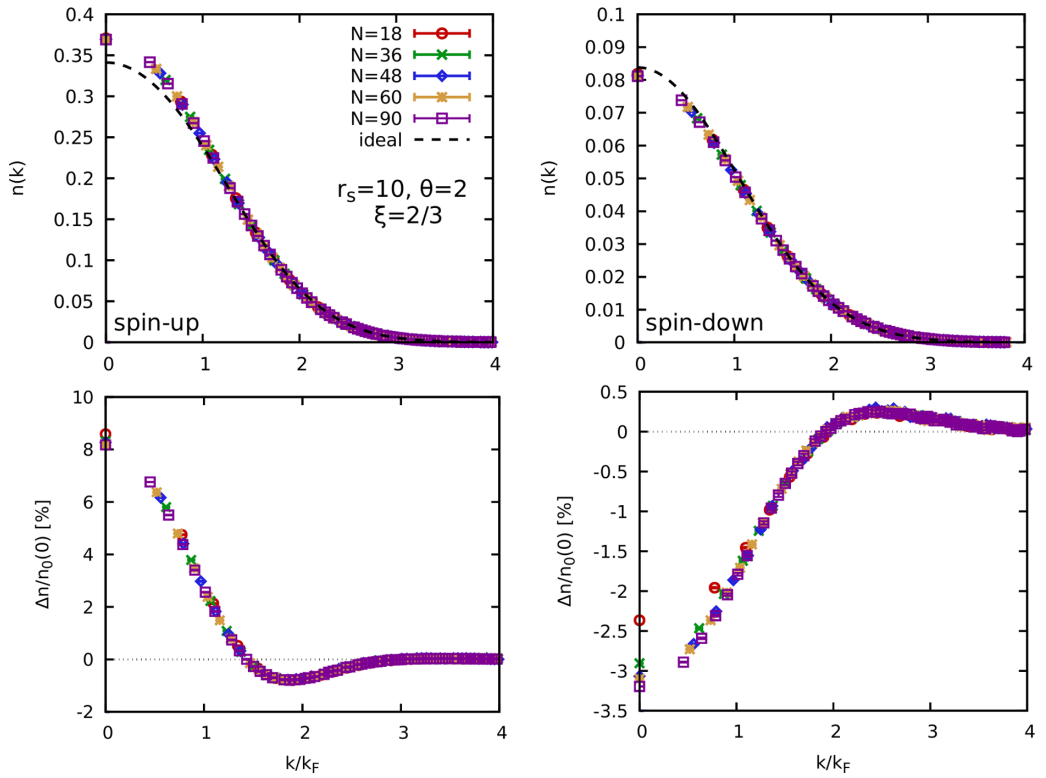

FIG. 6. Top: System-size dependence of the momentum distribution of the UEG at $r_s = 10$, $\theta = 2$, and $\xi = 2/3$. The left and right columns correspond to the spin-up and -down electrons, respectively. Bottom: Relative deviation between PIMC data for $n^\sigma(\mathbf{k})$ and the ideal Fermi distribution $n_0^\sigma(\mathbf{k})$ in percent, cf. Eq. (18). Note that we use the Fermi wave number of the unpolarized system $k_F^{\xi=0}$ as a reference.

Fig. 6 for $r_s = 10$ and $\theta_{\xi=0} = 2$ for $\xi = 2/3$. Note that we always use the reduced temperature $\theta_{\xi=0}$ of the unpolarized system as a reference throughout the remainder of this paper. We further mention that the selected polarization $\xi = 2/3$ constitutes a particularly relevant choice for the study of finite-size effects, as there are, by definition, always five times the number of spin-up compared to spin-down electrons. For example, we have $N^\uparrow = 50$ but only $N^\downarrow = 10$ for a total system size of $N = 60$ in this case. Since only electrons of the same spin-orientation exchange with each other, it is therefore reasonable to expect a different manifestation of finite-size effects in $n^\uparrow(\mathbf{k})$ and $n^\downarrow(\mathbf{k})$, which needs to be checked.

Let us start our investigation by considering results for $n^\uparrow(\mathbf{k})$ shown in the left column of Fig. 6, where the top and bottom panels show results for the momentum distribution itself and for the relative deviation to the ideal Fermi function [cf. Eq. (18)], respectively. More specifically, the different data points show our direct PIMC data that have been obtained for different values of N. Remarkably, we find hardly any dependence of $n^\uparrow(\mathbf{k})$ on the system size even for as few as $N = 18$ electrons. This can be seen particularly well in the bottom panel, where small deviations between the different data sets are noticeable only for small momenta. Still, even here these differences are clearly below 1%. From a physical perspective, we find a pronounced interaction-induced increase in $n^\uparrow(\mathbf{k})$ compared to $n_0^\uparrow(\mathbf{k})$, with a maximum of $\sim$8% at zero momentum.

Let us next consider the top right panel of Fig. 6, where we show our direct PIMC results for $n^\downarrow(\mathbf{k})$. Again, hardly any dependence on N can be resolved on this scale even for $N = 18$, where there are only $N^\downarrow = 3$ spin-down electrons within the simulation. The bottom panel of the same figure does reveal some systematic deviations for $N = 18$ and $N = 36$, but even the maximum finite-size effect is below 1%. In addition, we find that the occupation at small momenta is actually depleted compared to $n_0^\downarrow(\mathbf{k})$, which is in stark contrast to the behavior of the spin-up electrons observed in the left column of the same figure. A more detailed investigation of this effect is presented below.

Lastly, we show PIMC results for the off-diagonal density matrix in coordinate space $n(s)$ [cf. Eq. (4) above] in Fig. 7. Specifically, the left and right panels show results for spin-up and spin-down electrons, and the red circles, green crosses, and yellow stars correspond to $N = 18$, $N = 36$, and $N = 60$, respectively. Evidently, both $n^\uparrow(s)$ and $n^\downarrow(s)$ converge toward unity in the limit of $s \to 0$, as expected [86,88,94]. Furthermore, the off-diagonal density matrix is of an approximately Gaussian shape, and no oscillations can be found at large separations s. This negligible impact of permutation cycles involving a large number of particles further helps to explain the small manifestation of finite-size effects at these conditions.

While the small magnitude of the finite-size effects observed in Fig. 6 are certainly encouraging, it is expected from previous studies [64,69,115] that they might increase for higher densities. For this reason, we present a similar analysis for the same conditions at $r_s = 2$ in Fig. 8. Physically, this corresponds to a metallic density that is highly relevant to contemporary WDM research and can be realized

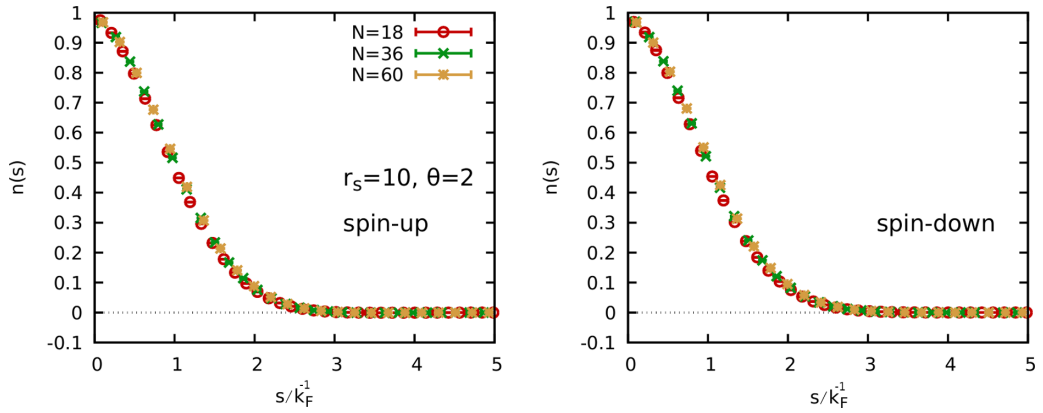

FIG. 7. Off-diagonal density matrix $n(s)$ [cf. Eq. (4)] of the UEG at $r_s = 10$, $\theta = 2$, and $\xi = 2/3$. The left and right panels show results for spin-up and spin-down electrons, and the red circles, green crosses, and yellow stars have been obtained for $N = 18$, $N = 36$, and $N = 60$, respectively.

experimentally for example with aluminum [75,117,118]. For completeness, we mention that the interpretation of the experiment in Ref. [117] remains a controversial topic. For example, even a basic plasma parameter such as the electronic temperature is still under debate [75,119]. While the present paper examines a similar density, it is not suitable to resolve these controversies and a new experiment is likely needed. In addition, we note that the smaller value of the coupling parameter r_s leads to a more pronounced impact of quantum degeneracy effects, which, in turn, results in a more severe fermion sign problem. This is conveniently characterized by the so-called *average sign* S (see, e.g., Ref. [101] for details), which constitutes a straightforward measure for the amount of cancellations of positive and negative terms within the simulation. In particular, the required computation time scales as $1/S^2$, such that a value of $S = 0.1$ would increase the CPU time by a factor of 100 compared to a PIMC simulation without a sign problem. For the system at hand, we find an average sign of $S \approx 0.01$ in the extended ensemble for $N = 60$ and $r_s = 2$, whereas it is $S \approx 0.4$ for $r_s = 10$. Therefore, PIMC simulations of $N = 90$ electrons are at present not computationally feasible at the higher density.

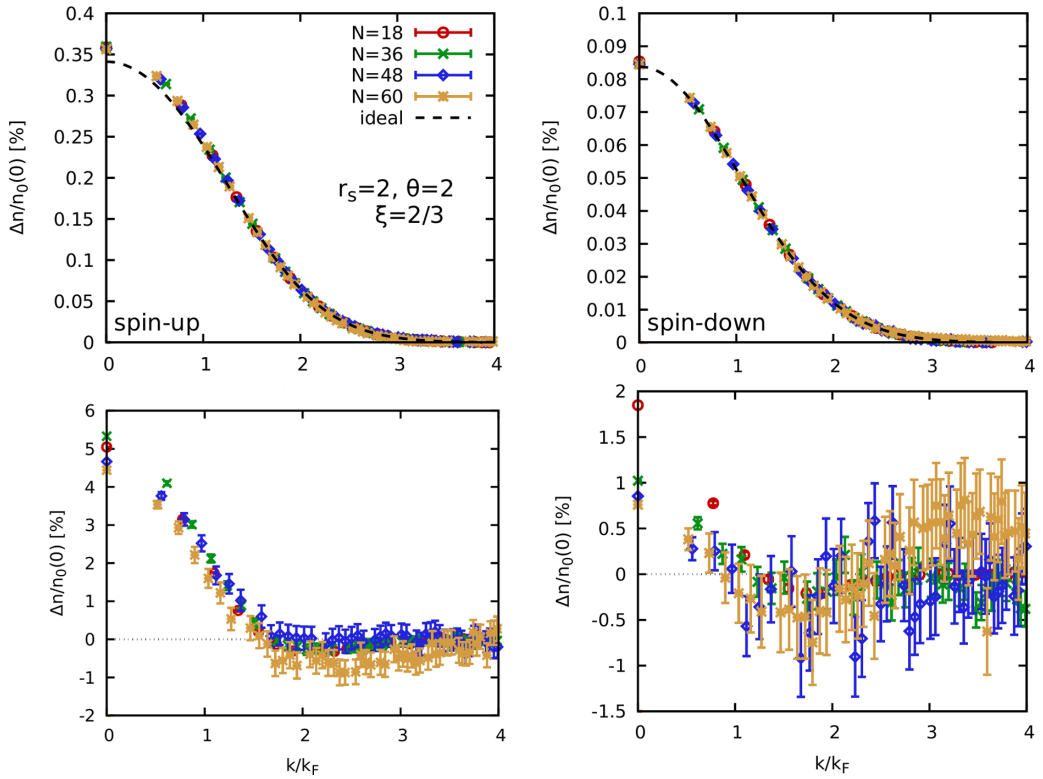

FIG. 8. Top: System-size dependence of the momentum distribution of the UEG at $r_s = 2$, $\theta = 2$, and $\xi = 2/3$. The left and right columns correspond to the spin-up and -down electrons, respectively. Bottom: Relative deviation between PIMC data for $n^\sigma(\mathbf{k})$ and the ideal Fermi distribution $n_0^\sigma(\mathbf{k})$ in percent, cf. Eq. (18). Note that we use the Fermi wave number of the unpolarized system $k_F^{\xi=0}$ as a reference.

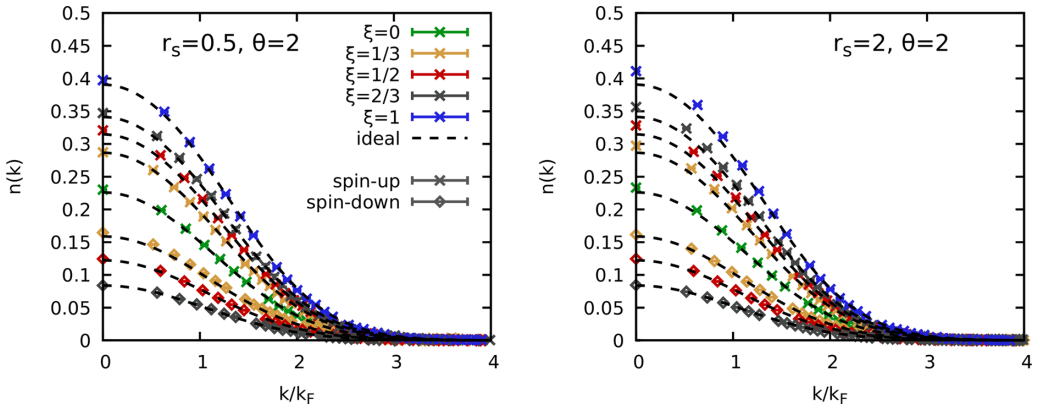

FIG. 9. Momentum distribution function $n^\sigma(\mathbf{k})$ for $\theta_{\xi=0} = 2$. Top left: $r_s = 0.5$; top right: $r_s = 2$; bottom left: $r_s = 4$; bottom right: $r_s = 10$. The colors distinguish different values of the spin-polarization ξ, and the dashed black curves show the corresponding results for the ideal Fermi gas $n_0^\sigma(\mathbf{k})$. Finally, the crosses and diamonds correspond to spin-up and spin-down electrons, respectively. Note that we use the Fermi wave number of the unpolarized system $k_F^{\xi=0}$ as a reference.

Returning to the topic of finite-size effects, again no deviations between the PIMC data sets for different N can be seen with the naked eye in the top row of Fig. 8 for either $n^\uparrow(\mathbf{k})$ or $n^\downarrow(\mathbf{k})$. The relative deviation to the ideal Fermi function shown in the bottom row allows for a more detailed perspective, where small differences between $N = 18$ and $N = 60$ of approximately 1% can be resolved for small momenta. In any case, it is safe to conclude that direct PIMC simulations with $N \sim 60$ electrons allow us to reliably estimate the main physical features of the momentum distribution function as finite-size effects are small at the conditions that are considered in this paper. For completeness, we mention that this changes at very low temperatures, where both the application of twisted boundary conditions [120,121] and an additional finite-size correction are required [122].

2. *Interplay of spin-polarization with density and temperature*

In the following, we will explicitly investigate the impact of the spin polarization on the momentum distribution $n(\mathbf{k})$ and its spin-resolved components $n^\uparrow(\mathbf{k})$ and $n^\downarrow(\mathbf{k})$. To ensure a better comparability, we will always compare results for the same temperature T for all ξ, thus resulting in different values of θ^σ [cf. Eq. (11)]. As a reference, we always give both θ and k_F for the case of a fully unpolarized system.

In Fig. 9, we show the momentum distribution function of the UEG at $\theta = 2$ for different values of ξ for $r_s = 0.5$ (left) and $r_s = 10$ (right). For $r_s = 0.5$, the PIMC data closely follow the ideal curves for all ξ as electronic correlation effects are comparably small. In addition, we observe the following monotonous ordering of $n^\sigma(\mathbf{k})$: Starting at $n^\uparrow(\mathbf{k}) = n^\downarrow(\mathbf{k})$ for the unpolarized case (green crosses), both the ideal curves and the PIMC data for the spin-up electrons monotonically increase with ξ. This is mainly a consequence of the increase in the number density $n^\uparrow$ (or, equivalently, the decrease in the density parameter $r_s^\uparrow$, cf. Fig. 2). Conversely, we find the opposite behavior for the spin-down electrons, with $n^\downarrow(\mathbf{k}) = 0$ in the limit of $\xi = 1$.

A less obvious question is the behavior of the total momentum distribution function $n(\mathbf{k}) = n^\uparrow(\mathbf{k}) + n^\downarrow(\mathbf{k})$, which we show in the left panel of Fig. 10 for these conditions. We note that the curves and data points for $\xi = 1/3$ and $\xi = 2/3$ have been omitted for better visibility. Interestingly, we observe the opposite ordering compared to $n^\uparrow(\mathbf{k})$ shown above, i.e., the largest value around zero momentum occurs for $\xi = 0$, both in the PIMC data and the ideal Fermi distribution function. This is a direct consequence of the fermionic antisymmetry under particle exchange and the resulting Pauli blocking and can be understood as follows: In the limit of $\xi = 1$, all electrons in the system are mutually affected by their common fermionic nature, which effectively pushes them toward larger momenta. In the opposite limit of $\xi = 0$, only half of the electrons mutually affect each other and, consequently, the fermionic push toward larger momenta is weaker. Naturally, $\xi = 1/2$ is located between these two extremes and, thus, located somewhere in the middle.

Let us next consider the impact of an increasing density parameter r_s on the spin-resolved components $n^\uparrow(\mathbf{k})$ and $n^\downarrow(\mathbf{k})$. This is shown in the right panel of Fig. 9 for the case of $r_s = 10$. Evidently, the effect of the coupling strength is most pronounced for the spin-up electrons, where, in particular, the occupation of the zero-momentum state is substantially increased compared to the ideal Fermi distribution. Further, we observe that this effect increases with ξ. The spin-down electrons, on the other hand, can hardly be distinguished from $n_0^\downarrow(\mathbf{k})$ with the naked eye on the depicted scale.

To get a more complete picture of the physics at play, we analyze the total momentum distribution $n(\mathbf{k})$ for $r_s = 10$ in the right panel of Fig. 10. As a direct consequence of the increased coupling strength, the electrons are more strongly spatially separated, and quantum degeneracy effects are less pronounced. Therefore, spin effects play a substantially smaller role in the direct PIMC data for the UEG than for the ideal curves. The large correlation-induced increase in $n^\uparrow(0)$ for large ξ is thus caused by the substantial spin dependence of $n_0(0)$, which is masked for the UEG by the Coulomb repulsion at low densities. Furthermore, the data for the UEG are closer to the unpolarized ideal curve than its polarized analog, as spin effects are less important for the ideal Fermi gas at $\xi = 0$ as well.

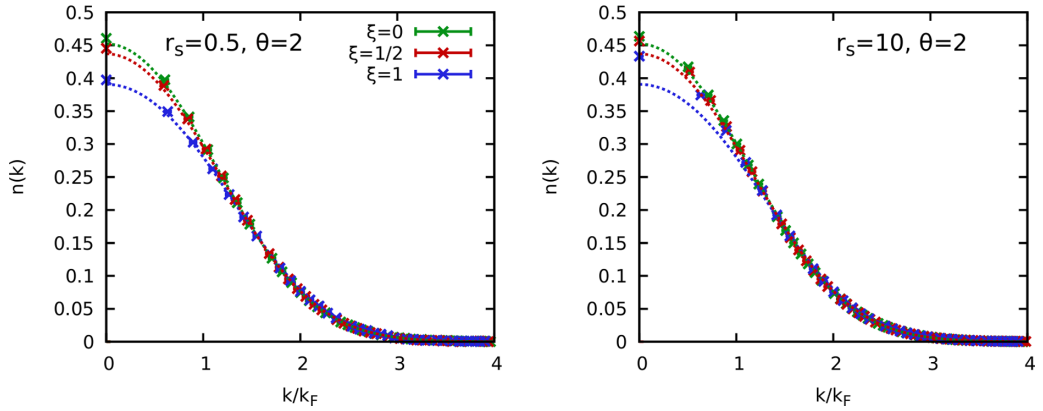

FIG. 10. Total momentum distribution function $n(\mathbf{k})$ at $\theta_{\xi=0} = 2$. Left: $r_s = 0.5$; right: $r_s = 10$. The colors distinguish different values of the spin-polarization ξ, and the corresponding dotted curves show results for the ideal Fermi gas $n_0^\sigma(\mathbf{k})$. Note that we use the Fermi wave number of the unpolarized system $k_F^{\xi=0}$ as a reference.

Let us next investigate the effect of the temperature on the spin dependence of the momentum distribution, which is analyzed in Fig. 11 for the metallic density of $r_s = 4$. The left column corresponds to $\theta_{\xi=0} = 1$ and the top panel shows results for the spin-resolved components $n^\uparrow(\mathbf{k})$ (crosses) and $n^\downarrow(\mathbf{k})$ (diamonds). Evidently, the reduction of the temperature by a factor of one half compared to Fig. 9 leads to a more pronounced difference in $n^\uparrow(0)$, in particular, for the fully ferromagnetic case. The spin-down electrons, on the other hand, are hardly affected by the Coulomb repulsion for $\xi > 0$. The bottom panel shows the corresponding results for the total momentum distribution $n(\mathbf{k})$, where again the impact of the spin-effects is less pronounced for the UEG compared to the ideal Fermi gas.

The right column of Fig. 11 shows the same investigation for a higher temperature, $\theta_{\xi=0} = 4$. First, we note that all curves are substantially broadened by thermal excitations, as expected. Furthermore, the correlation-induced increase in the zero momentum state is less pronounced than at lower temperatures and will eventually completely vanish in the

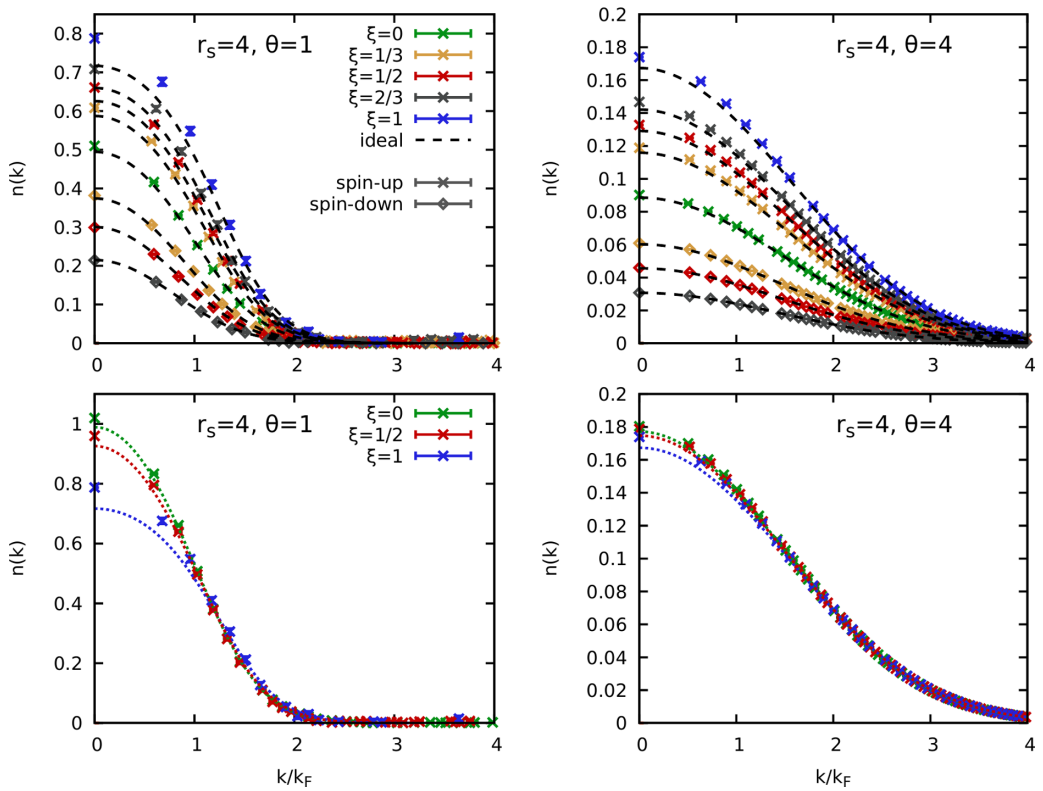

FIG. 11. Top: Spin-resolved momentum distribution function $n^\sigma(\mathbf{k})$ for $r_s = 2$. Left: $\theta_{\xi=0} = 1$; right: $\theta_{\xi=0} = 4$. The colors distinguish different values of the spin polarization ξ and the dashed black curves show the corresponding results for the ideal Fermi gas $n_0^\sigma(\mathbf{k})$. Finally, the crosses and diamonds correspond to spin-up and spin-down electrons, respectively. Bottom: Corresponding total momentum distributions $n(\mathbf{k}) = n^\uparrow(\mathbf{k}) + n^\downarrow(\mathbf{k})$. Note that we use the Fermi wave number of the unpolarized system $k_F^{\xi=0}$ as a reference.

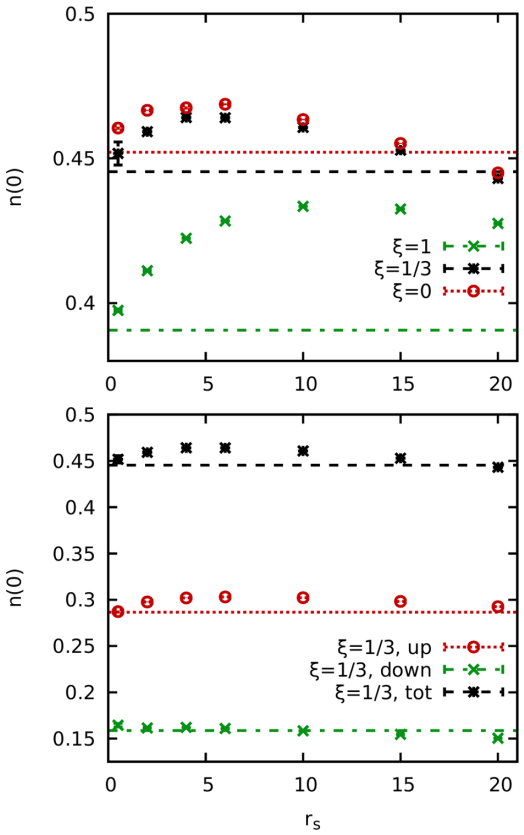

FIG. 12. Density dependence of the occupation at zero momentum $n(0)$ of the UEG at $\theta_{\xi=0} = 2$. Top panel: Direct PIMC data for the total momentum distribution $n(0) = n^{\uparrow}(0) + n^{\downarrow}(0)$ for $\xi = 0$ (red circles), $\xi = 1/3$ (black stars), and $\xi = 1$ (green crosses). The horizontal lines depict the corresponding ideal values $n_0(0)$. Bottom panel: Direct PIMC results for $\xi = 1/3$, black stars: $n(\mathbf{k})$; red circles: $n^{\uparrow}(\mathbf{k})$; green crosses: $n^{\downarrow}(\mathbf{k})$.

limit of large T when the system becomes increasingly ideal. Furthermore, $n^{\downarrow}(\mathbf{k})$ can hardly be distinguished from the corresponding ideal curves with the naked eye. Considering the total momentum distribution function $n(\mathbf{k})$ depicted in the bottom panel, we find that the deviations between the curves for the different values of ξ are substantially smaller compared to the cases of $\theta_{\xi=0} = 2$ and $\theta_{\xi=0} = 1$ both in the PIMC data for the UEG, and in the ideal results. This is expected as spin effects, too, will completely vanish in the limit of large temperatures, where the system becomes classical. In particular, $n(\mathbf{k})$ will converge toward the well-known Boltzmann distribution in this regime.

3. Zero-momentum occupation and exchange–correlation kinetic energy

Let us conclude our investigation with a more detailed study of the interaction-induced change in the occupation at zero momentum and the related lowering of the kinetic energy. As a first step, we show the density dependence of the total momentum distribution $n(0)$ at $\theta_{\xi=0}$ for three different values of the spin-polarization ξ in the top panel of Fig. 12. More specifically, the red circles, black stars, and green crosses show our direct PIMC data for the UEG for $\xi = 0$, $\xi = 1/3$,

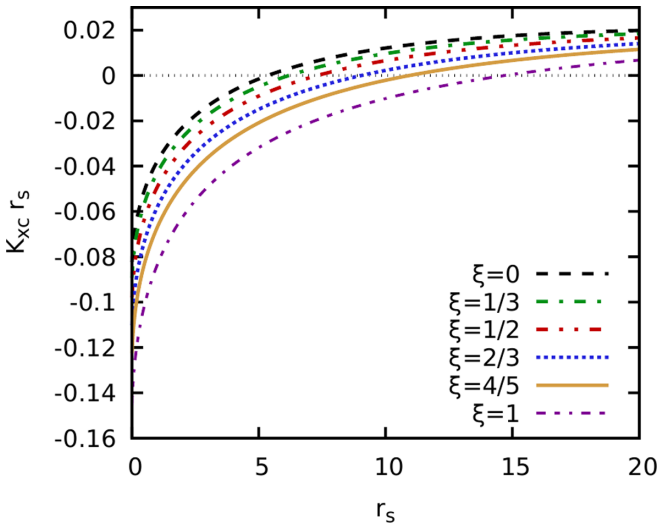

FIG. 13. Density dependence of the exchange–correlation part of the kinetic energy K_{xc} at $\theta_{\xi=0} = 2$ for different values of the spin polarization ξ evaluated from the parametrization of f_{xc} by Groth *et al.* [68] via Eq. (17).

and $\xi = 1$, respectively, and the horizontal lines depict the corresponding ideal values $n_0(0)$ that do not depend on the density. For small r_s, all three data sets exhibit a qualitatively similar behavior and monotonically increase starting from the ideal value at $r_s = 0$. In addition, the data points for $\xi = 0$ and $\xi = 1/3$ remain close to each other over the entire depicted r_s-range and almost agree with each other at $r_s = 20$. This is, of course, expected, as spin effects will eventually completely vanish at large r_s due to the increased coupling strength [11]. Furthermore, the PIMC results for $n(0)$ at $r_s = 20$ is below the ideal value for both of these spin polarizations, as the electrons are pushed toward larger momenta by the Coulomb coupling.

In contrast, the green crosses exhibit a related but clearly distinct progression. In particular, the interaction-induced increase in $n(0)$ is substantially larger compared to the other data sets and attains a maximum for $r_s \sim 10$. This has already been explained above by the more pronounced spin dependence of $n_0(0)$ compared to $n(0)$ of the UEG and is thus directly caused by the large gap between the respective Fermi functions for the different values of ξ.

For completeness, we also show the r_s dependence of the spin-resolved components of the momentum distribution functions $n^{\uparrow}(0)$ and $n^{\downarrow}(0)$ at $\xi = 1/3$ in the bottom panel of Fig. 12. This plot further substantiates our previous findings that the correlation-induced increase in the occupation of the zero-momentum state is mostly caused by the spin-up electrons. In addition, we find that the PIMC data for $n^{\downarrow}(0)$ are actually smaller than $n_0^{\downarrow}(0)$ for $r_s \gtrsim 10$, whereas the opposite still holds for $n^{\uparrow}(0)$. A possible explanation for this effect is given by the comparably increased spin-resolved density parameter $r_s^{\downarrow}$ shown in Fig. 2 above.

Let us next consider Fig. 13, where we show the density dependence of the exchange–correlation part to the kinetic energy K_{xc} (obtained by evaluating Eq. (17) using as input the parametrization of f_{xc} by Groth *et al.* [68]) for different values of the spin-polarization ξ. First and foremost, we note the similar progression of $K_{\mathrm{xc}} \cdot r_s$ for all ξ, which attain a finite

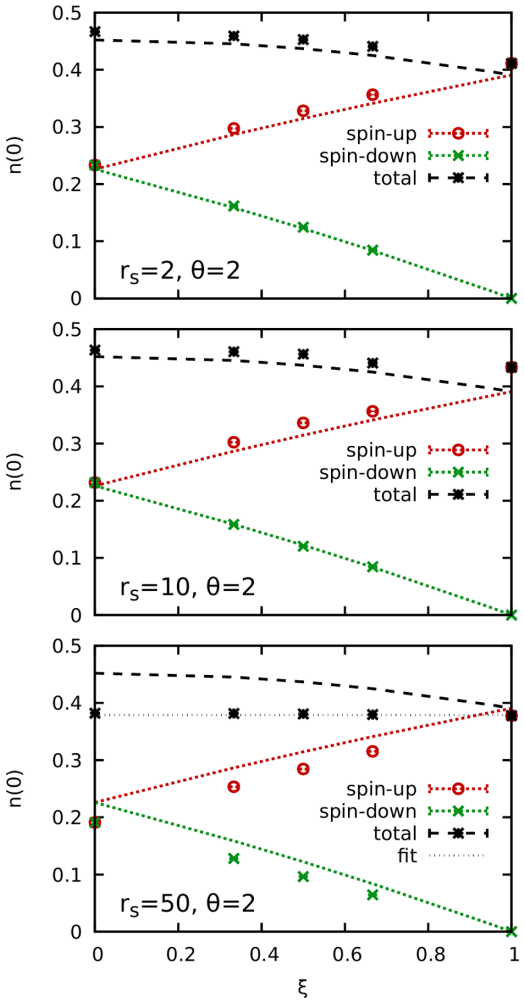

FIG. 14. Polarization dependence of the occupation at zero momentum for $r_s = 2$ (top), $r_s = 10$ (center), and $r_s = 50$ (bottom) at $\theta_{\xi=0} = 2$. The red circles, green crosses, and black stars correspond to the spin-up component $n^{\uparrow}(0)$, spin-down component $n^{\downarrow}(0)$, and the total distribution function $n(0)$, respectively. The corresponding lines show the respective ideal Fermi distribution function.

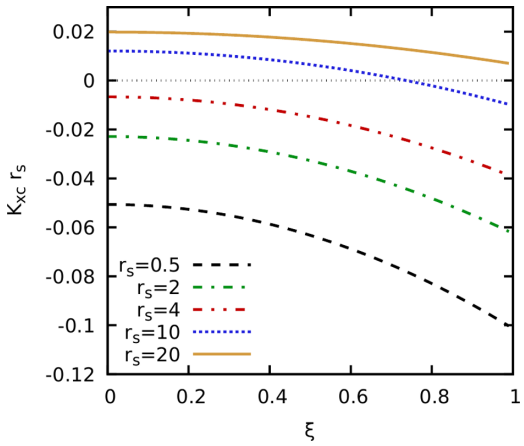

FIG. 15. Polarization dependence of the exchange–correlation contribution to the kinetic energy $K_{\rm xc}$ at $\theta_{\xi=0} = 2$ evaluated from the parametrization of $f_{\rm xc}$ by Groth *et al.* [68] via Eq. (17). The different lines correspond to various values of the density parameter r_s.

negative value in the limit of $r_s \to 0$, monotonously increase with r_s, and eventually become positive. In addition, we find a strict ordering of these curves with ξ, and the distancing between individual curves increases with the spin polarization. This is again directly caused by the comparably larger spin dependence of the ideal energy E_0 for large ξ, whereas the actual kinetic energy K of the UEG is less affected by the spin, and thus more closely resembles E_0 for the unpolarized case. From a physical perspective, we note that the behavior observed in Fig. 13 might indicate a substantial *negative tail* at large momenta in the static local field correction of the ferromagnetic UEG at WDM conditions. This prediction can be verified by independent PIMC simulations of the spin-polarized UEG, which constitutes an interesting project for future research.

The final investigation to be presented in this paper is the dependence of the occupation at zero momentum on the spin-polarization with both the density and the temperature being kept constant. This is shown in Fig. 14 for $\theta_{\xi=0}$ and three different values of the density parameter r_s. In particular, the top panel shows results for $r_s = 2$ and the red circles, green stars, and black crosses correspond to the spin-up component $n^{\uparrow}(0)$, spin-down component $n^{\downarrow}(0)$, and the total momentum distribution $n(0)$. Most obviously, both the individual spin-up and spin-down components strongly depend on ξ, which is a direct consequence of the corresponding relative shift in the number densities $n^{\uparrow}$ and $n^{\downarrow}$. Furthermore, the total distribution $n(0)$ also noticeably depends on ξ both for the ideal and the interacting case, and monotonically decreases with ξ. The physical origin of this effect is the increased impact of the Pauli blocking between electrons of the same species, which pushes the occupation toward large momenta. Finally, we again find that the correlation-induced increase in $n(0)$ is nearly exclusively due to $n^{\uparrow}(0)$, as it is by now expected.

The center panel of Fig. 14 shows the same information for a larger value of the coupling strength, $r_s = 10$. Overall, the results are qualitatively quite similar to the $r_s = 2$ case shown in the top panel, but the difference between $n(0)$ and $n_0(0)$ is significantly increased at $\xi = 1$ as the spin-effects are effectively masked in the UEG by the Coulomb repulsion.

Lastly, the bottom panel shows results for strongly coupled electron liquid regime, $r_s = 50$. In this case, the strong Coulomb coupling almost completely removes the dependence of the PIMC data for the total momentum distribution function on the spin polarization, and the corresponding black stars are well reproduced by a constant fit (dotted grey line). In addition, both spin components exhibit a decreased occupation at zero momentum compared to the ideal Fermi function over the entire ξ range.

Let us conclude our investigation with an analysis of the ξ dependence of the exchange–correlation kinetic energy $K_{\rm xc}$. To this end, we again compute $K_{\rm xc}$ via Eq. (17) from the accurate parametrization by Groth *et al.* [68], and the results are shown in Fig. 15. Overall, the relative spin dependence is substantial for all depicted values of the density parameter r_s and is of the order of 100%. Even at $r_s = 20$, where most physical observables of the UEG like the total energy K only weakly depend on ξ, the strong ξ dependence of E_0 is directly

reflected in Eq. (16). In the WDM regime ($r_s = 0.5, 2, 4$), we find substantially larger values for $K_{\rm xc}$ for the ferromagnetic case, which might be directly reflected in important material properties like the static local field correction [73,74,113]. In particular, a pronounced *negative tail* of the local field correction at intermediate to large wave numbers could have a noticeable impact on the spectral properties [9,73,79–81] of the system, with potentially important implications for x-ray Thomson scattering applications [123].

IV. SUMMARY AND DISCUSSION

In summary, we have presented an extensive study of the impact of spin effects on the momentum distribution function $n(\mathbf{k})$ and related properties. This has been achieved on the basis of extensive direct PIMC simulations for different densities r_s, temperatures θ, and degrees of the spin polarization ξ. Our central findings can be concisely summarized as follows: (i) the correlation-induced increase in the occupation of the zero-momentum state $n(\mathbf{0})$ substantially depends on the spin-polarization ξ, which is mainly a consequence of the spin dependence of the ideal Fermi function n_0; (ii) previous RPIMC data for $n(\mathbf{k})$ by Militzer *et al.* [86] are afflicted with a systematic error, which is a consequence of the determination of the normalization and not a consequence of the employed fixed-node approximation; (iii) finite-size effects in our PIMC data only manifest for small k and hardly exceed 1% for both $n^{\uparrow}(\mathbf{k})$ and $n^{\downarrow}(\mathbf{k})$; (iv) the interaction-induced increase in $n(\mathbf{0})$ is mainly facilitated by the spin-up electrons (majority electrons), which can be explained in terms of the spin-resolved reduced parameters $r_s^{\downarrow}$ and $\theta^{\downarrow}$; and, finally, (v) both the shift in the occupation of the zero-momentum state and the exchange–correlation part of the kinetic energy strongly depend on the spin-polarization even in the limit of the strongly correlated electron liquid ($r_s = 50$), which can again be traced back to the ξ dependence of the noninteracting reference system.

Let us conclude this discussion by outlining a few directions for future investigations. First, we mention that our extensive set of direct PIMC data are freely available online [124] and can be used as an accurate benchmark for the development of methods and approximations or as input for parametrizations. Furthermore, we reiterate the high importance of the momentum distribution function of electrons for the description of transport properties of WDM in an external magnetic field [90]. With respect to the UEG itself, the numerical investigation of the large-momentum tail of $n(\mathbf{k})$ [cf. Eq. (15)] in the fully polarized case will further advance or current understanding of this fundamental model system, but remains out of reach for PIMC methods operating in coordinate space. In contrast, Hunger *et al.* [87] have recently demonstrated that the configuration PIMC method (which directly operates in $\mathbf{k}$ space) is capable to resolve the required 8–10 orders of magnitude in $n(\mathbf{k})$, and its application to the spin-polarized case, thus, constitutes an enticing possibility. Finally, the substantially negative values of $K_{\rm xc}$ for large ξ that have been reported in this paper potentially indicate a pronounced negative tail for large wave numbers in the static local field correction of the ferromagnetic UEG. Yet previous PIMC studies of such linear-response properties have been limited to $\xi = 0$, and an extension of these efforts to other values of ξ is highly desirable.

A repository containing all PIMC raw data will be made available upon publication, see Supplemental Material Ref. [124].

ACKNOWLEDGMENTS

This paper was partly funded by the Center of Advanced Systems Understanding (CASUS) which is financed by Germany's Federal Ministry of Education and Research (BMBF) and by the Saxon Ministry for Science, Culture and Tourism (SMWK) with tax funds on the basis of the budget approved by the Saxon State Parliament. B.M. acknowledges support from the U.S. National Nuclear Security Administration (Grant No. DE-NA0003842). The PIMC calculations were carried out at the Norddeutscher Verbund für Hoch- und Höchstleistungsrechnen (HLRN) under Grant No. shp00026 and on a Bull Cluster at the Center for Information Services and High Performance Computing (ZIH) at Technische Universität Dresden.

[1] P.-F. Loos and P. M. W. Gill, The uniform electron gas, Comput. Mol. Sci. **6**, 410 (2016).

[2] G. Giuliani and G. Vignale, *Quantum Theory of the Electron Liquid* (Cambridge University Press, Cambridge, 2008).

[3] J. Bardeen, L. N. Cooper, and J. R. Schrieffer, Theory of superconductivity, Phys. Rev. **108**, 1175 (1957).

[4] D. Bohm and A. D. Pines, Collective description of electron interactions: II. Collective vs individual particle aspects of the interactions, Phys. Rev. **85**, 338 (1952).

[5] N. D. Drummond, Z. Radnai, J. R. Trail, M. D. Towler, and R. J. Needs, Diffusion quantum Monte Carlo study of three-dimensional Wigner crystals, Phys. Rev. B **69**, 085116 (2004).

[6] M. D. Jones and D. M. Ceperley, Crystallization of the One-Component Plasma at Finite Temperature, Phys. Rev. Lett. **76**, 4572 (1996).

[7] Y. Takada and H. Yasuhara, Dynamical Structure Factor of the Homogeneous Electron Liquid: Its Accurate Shape and the Interpretation of Experiments on Aluminum, Phys. Rev. Lett. **89**, 216402 (2002).

[8] Y. Takada, Emergence of an excitonic collective mode in the dilute electron gas, Phys. Rev. B **94**, 245106 (2016).

[9] T. Dornheim, S. Groth, J. Vorberger, and M. Bonitz, *Ab Initio* Path Integral Monte Carlo Results for the Dynamic Structure Factor of Correlated Electrons: From the Electron Liquid to Warm Dense Matter, Phys. Rev. Lett. **121**, 255001 (2018).

[10] H. K. Schweng and H. M. Böhm, Finite-temperature electron correlations in the framework of a dynamic local-field correction, Phys. Rev. B **48**, 2037 (1993).

[11] T. Dornheim, T. Sjostrom, S. Tanaka, and J. Vorberger, Strongly coupled electron liquid: Ab initio path integral Monte Carlo simulations and dielectric theories, Phys. Rev. B **101**, 045129 (2020).

[12] D. M. Ceperley and B. J. Alder, Ground State of the Electron Gas by a Stochastic Method, Phys. Rev. Lett. **45**, 566 (1980).

[13] S. Moroni, D. M. Ceperley, and G. Senatore, Static Response and Local Field Factor of the Electron Gas, Phys. Rev. Lett. **75**, 689 (1995).

[14] R. O. Jones, Density functional theory: Its origins, rise to prominence, and future, Rev. Mod. Phys. **87**, 897 (2015).

[15] V. E. Fortov, Extreme states of matter on earth and in space, Phys.-Usp. **52**, 615 (2009).

[16] A. Benuzzi-Mounaix, S. Mazevet, A. Ravasio, T. Vinci, A. Denoeud, M. Koenig, N. Amadou, E. Brambrink, F. Festa, A. Levy, M. Harmand, S. Brygoo, G. Huser, V. Recoules, J. Bouchet, G. Morard, F. Guyot, T. de Resseguier, K. Myanishi, N. Ozaki *et al.*, Progress in warm dense matter study with applications to planetology, Phys. Scr. **2014**, 014060 (2014).

[17] N. Nettelmann, R. Redmer, and D. Blaschke, Warm dense matter in giant planets and exoplanets, Phys. Part. Nuclei **39**, 1122 (2008).

[18] B. Militzer, W. B. Hubbard, J. Vorberger, I. Tamblyn, and S. A. Bonev, A massive core in Jupiter predicted from first-principles simulations, Astrophys. J. **688**, L45 (2008).

[19] J. Vorberger, I. Tamblyn, B. Militzer, and S. A. Bonev, Hydrogen-helium mixtures in the interiors of giant planets, Phys. Rev. B **75**, 024206 (2007).

[20] D. Saumon, W. B. Hubbard, G. Chabrier, and H. M. van Horn, The role of the molecular-metallic transition of hydrogen in the evolution of Jupiter, Saturn, and brown dwarfs, Astrophys. J **391**, 827 (1992).

[21] A. Becker, W. Lorenzen, J. J. Fortney, N. Nettelmann, M. Schöttler, and R. Redmer, Ab initio equations of state for hydrogen (h-reos.3) and helium (he-reos.3) and their implications for the interior of brown dwarfs, Astrophys. J. Suppl. Ser **215**, 21 (2014).

[22] N. Chamel and P. Haensel, Physics of neutron star crusts, Living Rev. Relativity **11**, 10 (2008).

[23] S. X. Hu, B. Militzer, V. N. Goncharov, and S. Skupsky, First-principles equation-of-state table of deuterium for inertial confinement fusion applications, Phys. Rev. B **84**, 224109 (2011).

[24] M. L. Brongersma, N. J. Halas, and P. Nordlander, Plasmon-induced hot carrier science and technology, Nat. Nanotechnol. **10**, 25 (2015).

[25] D. Kraus, A. Ravasio, M. Gauthier, D. O. Gericke, J. Vorberger, S. Frydrych, J. Helfrich, L. B. Fletcher, G. Schaumann, B. Nagler, B. Barbrel, B. Bachmann, E. J. Gamboa, S. Göde, E. Granados, G. Gregori, H. J. Lee, P. Neumayer, W. Schumaker, T. Döppner *et al.*, Nanosecond formation of diamond and lonsdaleite by shock compression of graphite, Nat. Commun. **7**, 10970 (2016).

[26] D. Kraus, J. Vorberger, A. Pak, N. J. Hartley, L. B. Fletcher, S. Frydrych, E. Galtier, E. J. Gamboa, D. O. Gericke, S. H. Glenzer, E. Granados, M. J. MacDonald, A. J. MacKinnon, E. E. McBride, I. Nam, P. Neumayer, M. Roth, A. M. Saunders, A. K. Schuster, P. Sun *et al.*, Formation of diamonds in laser-compressed hydrocarbons at planetary interior conditions, Nat. Astron. **1**, 606 (2017).

[27] A. Lazicki, D. McGonegle, J. R. Rygg, D. G. Braun, D. C. Swift, M. G. Gorman, R. F. Smith, P. G. Heighway, A. Higginbotham, M. J. Suggit, D. E. Fratanduono, F. Coppari, C. E. Wehrenberg, R. G. Kraus, D. Erskine, J. V. Bernier, J. M. McNaney, R. E. Rudd, G. W. Collins, J. H. Eggert *et al.*, Metastability of diamond ramp-compressed to 2 terapascals, Nature (London) **589**, 532 (2021).

[28] T. Ott, H. Thomsen, J. W. Abraham, T. Dornheim, and M. Bonitz, Recent progress in the theory and simulation of strongly correlated plasmas: phase transitions, transport, quantum, and magnetic field effects, Eur. Phys. J. D **72**, 84 (2018).

[29] M. Bonitz, T. Dornheim, Zh. A. Moldabekov, S. Zhang, P. Hamann, H. Kählert, A. Filinov, K. Ramakrishna, and J. Vorberger, Ab initio simulation of warm dense matter, Phys. Plasmas **27**, 042710 (2020).

[30] *Frontiers and Challenges in Warm Dense Matter*, edited by F. Graziani, M. P. Desjarlais, R. Redmer, and S. B. Trickey (Springer International Publishing, Heidelberg, Germany, 2014).

[31] V. V. Karasiev, L. Calderin, and S. B. Trickey, Importance of finite-temperature exchange correlation for warm dense matter calculations, Phys. Rev. E **93**, 063207 (2016).

[32] K. Ramakrishna, T. Dornheim, and J. Vorberger, Influence of finite temperature exchange-correlation effects in hydrogen, Phys. Rev. B **101**, 195129 (2020).

[33] T. Sjostrom and J. Daligault, Gradient corrections to the exchange-correlation free energy, Phys. Rev. B **90**, 155109 (2014).

[34] K. S. Singwi, M. P. Tosi, R. H. Land, and A. Sjölander, Electron correlations at metallic densities, Phys. Rev. **176**, 589 (1968).

[35] P. Vashishta and K. S. Singwi, Electron correlations at metallic densities. V, Phys. Rev. B **6**, 875 (1972).

[36] S. Tanaka and S. Ichimaru, Thermodynamics and correlational properties of finite-temperature electron liquids in the Singwi-Tosi-Land-Sjölander approximation, J. Phys. Soc. Jpn. **55**, 2278 (1986).

[37] S. Ichimaru, H. Iyetomi, and S. Tanaka, Statistical physics of dense plasmas: Thermodynamics, transport coefficients and dynamic correlations, Phys. Rep. **149**, 91 (1987).

[38] W. Stolzmann and M. Rösler, Static local-field corrected dielectric and thermodynamic functions, Contrib. Plasma Phys **41**, 203 (2001).

[39] T. Sjostrom and J. Dufty, Uniform electron gas at finite temperatures, Phys. Rev. B **88**, 115123 (2013).

[40] P. Arora, K. Kumar, and R. K. Moudgil, Spin-resolved correlations in the warm-dense homogeneous electron gas, Eur. Phys. J. B **90**, 76 (2017).

[41] F. L. Castello, P. Tolias, and T. Dornheim, Classical bridge functions in classical and quantum plasma liquids, arXiv:2107.03537.

[42] S. Tanaka, Correlational and thermodynamic properties of finite-temperature electron liquids in the hypernetted-chain approximation, J. Chem. Phys. **145**, 214104 (2016).

[43] Zh. A. Moldabekov, T. Dornheim, M. Bonitz, and T. S. Ramazanov, Ion energy-loss characteristics and friction in a free-electron gas at warm dense matter and nonideal dense plasma conditions, Phys. Rev. E **101**, 053203 (2020).

[44] S. Ichimaru, Nuclear fusion in dense plasmas, Rev. Mod. Phys. **65**, 255 (1993).

[45] F. Perrot and M. W. C. Dharma-wardana, Exchange and correlation potentials for electron-ion systems at finite temperatures, Phys. Rev. A **30**, 2619 (1984).

[46] W. D. Kraeft and W. Stolzmann, Thermodynamic functions of Coulomb systems, Physica A **97**, 306 (1979).

[47] W. D. Kraeft, M. Schlanges, J. Vorberger, and H. E. DeWitt, Kinetic and correlation energies and distribution functions of dense plasmas, Phys. Rev. E **66**, 046405 (2002).
[48] F. Perrot and M. W. C. Dharma-wardana, Spin-polarized electron liquid at arbitrary temperatures: Exchange-correlation energies, electron-distribution functions, and the static response functions, Phys. Rev. B **62**, 16536 (2000).
[49] M. W. C. Dharma-wardana and F. Perrot, Simple Classical Mapping of the Spin-Polarized Quantum Electron Gas: Distribution Functions and Local-Field Corrections, Phys. Rev. Lett. **84**, 959 (2000).
[50] S. Dutta and J. Dufty, Uniform electron gas at warm, dense matter conditions, Europhys. Lett. **102**, 67005 (2013).
[51] Y. Liu and J. Wu, An improved classical mapping method for homogeneous electron gases at finite temperature, J. Chem. Phys. **141**, 064115 (2014).
[52] N.-H. Kwong and M. Bonitz, Real-Time Kadanoff-Baym Approach to Plasma Oscillations in a Correlated Electron Gas, Phys. Rev. Lett. **84**, 1768 (2000).
[53] J. J. Kas and J. J. Rehr, Finite Temperature Green's Function Approach for Excited State and Thermodynamic Properties of Cool to Warm Dense Matter, Phys. Rev. Lett. **119**, 176403 (2017).
[54] E. W. Brown, B. K. Clark, J. L. DuBois, and D. M. Ceperley, Path-Integral Monte Carlo Simulation of the Warm Dense Homogeneous Electron Gas, Phys. Rev. Lett. **110**, 146405 (2013).
[55] N. S. Blunt, T. W. Rogers, J. S. Spencer, and W. M. C. Foulkes, Density-matrix quantum Monte Carlo method, Phys. Rev. B **89**, 245124 (2014).
[56] T. Schoof, S. Groth, J. Vorberger, and M. Bonitz, Ab Initio Thermodynamic Results for the Degenerate Electron Gas at Finite Temperature, Phys. Rev. Lett. **115**, 130402 (2015).
[57] F. D. Malone, N. S. Blunt, J. J. Shepherd, D. K. K. Lee, J. S. Spencer, and W. M. C. Foulkes, Interaction picture density matrix quantum Monte Carlo, J. Chem. Phys. **143**, 044116 (2015).
[58] T. Dornheim, S. Groth, A. Filinov, and M. Bonitz, Permutation blocking path integral Monte Carlo: a highly efficient approach to the simulation of strongly degenerate non-ideal fermions, New J. Phys. **17**, 073017 (2015).
[59] T. Dornheim, T. Schoof, S. Groth, A. Filinov, and M. Bonitz, Permutation blocking path integral Monte Carlo approach to the uniform electron gas at finite temperature, J. Chem. Phys. **143**, 204101 (2015).
[60] S. Groth, T. Schoof, T. Dornheim, and M. Bonitz, Ab initio quantum Monte Carlo simulations of the uniform electron gas without fixed nodes, Phys. Rev. B **93**, 085102 (2016).
[61] F. D. Malone, N. S. Blunt, E. W. Brown, D. K. K. Lee, J. S. Spencer, W. M. C. Foulkes, and J. J. Shepherd, Accurate Exchange-Correlation Energies for the Warm Dense Electron Gas, Phys. Rev. Lett. **117**, 115701 (2016).
[62] Y. Liu, M. Cho, and B. Rubenstein, Ab initio finite temperature auxiliary field quantum Monte Carlo, J. Chem. Theory Comput. **14**, 4722 (2018).
[63] J. Lee, M. A. Morales, and F. D. Malone, A phaseless auxiliary-field quantum Monte Carlo perspective on the uniform electron gas at finite temperatures: Issues, observations, and benchmark study, J. Chem. Phys. **154**, 064109 (2021).
[64] T. Dornheim, S. Groth, T. Sjostrom, F. D. Malone, W. M. C. Foulkes, and M. Bonitz, Ab Initio Quantum Monte Carlo Simulation of the Warm Dense Electron Gas in the Thermodynamic Limit, Phys. Rev. Lett. **117**, 156403 (2016).
[65] A. Yilmaz, K. Hunger, T. Dornheim, S. Groth, and M. Bonitz, Restricted configuration path integral Monte Carlo, J. Chem. Phys. **153**, 124114 (2020).
[66] T. Dornheim, S. Groth, F. D. Malone, T. Schoof, T. Sjostrom, W. M. C. Foulkes, and M. Bonitz, Ab initio quantum Monte Carlo simulation of the warm dense electron gas, Phys. Plasmas **24**, 056303 (2017).
[67] V. V. Karasiev, T. Sjostrom, J. Dufty, and S. B. Trickey, Accurate Homogeneous Electron Gas Exchange-Correlation Free Energy for Local Spin-Density Calculations, Phys. Rev. Lett. **112**, 076403 (2014).
[68] S. Groth, T. Dornheim, T. Sjostrom, F. D. Malone, W. M. C. Foulkes, and M. Bonitz, Ab Initio Exchange–Correlation Free Energy of the Uniform Electron Gas at Warm Dense Matter Conditions, Phys. Rev. Lett. **119**, 135001 (2017).
[69] T. Dornheim, S. Groth, and M. Bonitz, The uniform electron gas at warm dense matter conditions, Phys. Rep. **744**, 1 (2018).
[70] V. V. Karasiev, S. B. Trickey, and J. W. Dufty, Status of free-energy representations for the homogeneous electron gas, Phys. Rev. B **99**, 195134 (2019).
[71] V. V. Karasiev, J. W. Dufty, and S. B. Trickey, Nonempirical Semilocal Free-Energy Density Functional for Matter Under Extreme Conditions, Phys. Rev. Lett. **120**, 076401 (2018).
[72] D. I. Mihaylov, V. V. Karasiev, and S. X. Hu, Thermal hybrid exchange-correlation density functional for improving the description of warm dense matter, Phys. Rev. B **101**, 245141 (2020).
[73] S. Groth, T. Dornheim, and J. Vorberger, Ab initio path integral Monte Carlo approach to the static and dynamic density response of the uniform electron gas, Phys. Rev. B **99**, 235122 (2019).
[74] T. Dornheim, J. Vorberger, S. Groth, N. Hoffmann, Zh.A. Moldabekov, and M. Bonitz, The static local field correction of the warm dense electron gas: An ab initio path integral Monte Carlo study and machine learning representation, J. Chem. Phys. **151**, 194104 (2019).
[75] T. Dornheim, A. Cangi, K. Ramakrishna, M. Böhme, S. Tanaka, and J. Vorberger, Effective Static Approximation: A Fast and Reliable Tool for Warm-Dense Matter Theory, Phys. Rev. Lett. **125**, 235001 (2020).
[76] T. Dornheim, Z. A. Moldabekov, and P. Tolias, Analytical representation of the local field correction of the uniform electron gas within the effective static approximation, Phys. Rev. B **103**, 165102 (2021).
[77] T. Dornheim, J. Vorberger, and M. Bonitz, Nonlinear Electronic Density Response in Warm Dense Matter, Phys. Rev. Lett. **125**, 085001 (2020).
[78] T. Dornheim, M. Böhme, Z. A. Moldabekov, J. Vorberger, and M. Bonitz, Density response of the warm dense electron gas beyond linear response theory: Excitation of harmonics, Phys. Rev. Research **3**, 033231 (2021).
[79] T. Dornheim and J. Vorberger, Finite-size effects in the reconstruction of dynamic properties from ab initio path integral Monte Carlo simulations, Phys. Rev. E **102**, 063301 (2020).
[80] P. Hamann, J. Vorberger, T. Dornheim, Z. A. Moldabekov, and M. Bonitz, Ab initio results for the plasmon dispersion and damping of the warm dense electron gas, Contrib. Plasma Phys. **60**, e202000147 (2020).

[81] P. Hamann, T. Dornheim, J. Vorberger, Z. A. Moldabekov, and M. Bonitz, Dynamic properties of the warm dense electron gas based on *abinitio* path integral Monte Carlo simulations, Phys. Rev. B **102**, 125150 (2020).

[82] K. G. Lynn, J. R. MacDonald, R. A. Boie, L. C. Feldman, J. D. Gabbe, M. F. Robbins, E. Bonderup, and J. Golovchenko, Positron-Annihilation Momentum Profiles in Aluminum: Core Contribution and the Independent-Particle Model, Phys. Rev. Lett. **38**, 241 (1977).

[83] P.C. Jain, R.M. Singru, and K.P. Gopinathan, *Positron Annihilation: Proceedings of the Seventh International Conference on Positron Annihilation, New Delhi, India, January 6-11, 1985*; Edited by P. C. Jain, R. M. Singru, K. P. Gopinathan (World Scientific, Singapore, 1985).

[84] S. Rightley and S. D. Baalrud, Kinetic model for electron-ion transport in warm dense matter, Phys. Rev. E **103**, 063206 (2021).

[85] B. Militzer and E. L. Pollock, Lowering of the Kinetic Energy in Interacting Quantum Systems, Phys. Rev. Lett. **89**, 280401 (2002).

[86] B. Militzer, E. L. Pollock, and D. M. Ceperley, Path integral Monte Carlo calculation of the momentum distribution of the homogeneous electron gas at finite temperature, High Energy Density Phys. **30**, 13 (2019).

[87] K. Hunger, T. Schoof, T. Dornheim, M. Bonitz, and A. Filinov, Momentum distribution function and short-range correlations of the warm dense electron gas: Ab initio quantum Monte Carlo results, Phys. Rev. E **103**, 053204 (2021).

[88] T. Dornheim, M. Böhme, B. Militzer, and J. Vorberger, Ab initio path integral Monte Carlo approach to the momentum distribution of the uniform electron gas at finite temperature without fixed nodes, Phys. Rev. B **103**, 205142 (2021).

[89] E. M. Lifshitz and L. P. Pitaevski, *Physical Kinetics* (Pergamon, Oxford, 1981).

[90] P. Haensel, A. Y. Potekhin, and D.G. Yakovlev, *Neutron Stars 1: Equation of State and Structure* (Springer, New York, 2006).

[91] L. J. Perkins, B. G. Logan, G. B. Zimmerman, and C. J. Werner, Two-dimensional simulations of thermonuclear burn in ignition-scale inertial confinement fusion targets under compressed axial magnetic fields, Phys. Plasmas **20**, 072708 (2013).

[92] B. Appelbe, A. L. Velikovich, M. Sherlock, C. Walsh, A. Crilly, S. O' Neill, and J. Chittenden, Magnetic field transport in propagating thermonuclear burn, Phys. Plasmas **28**, 032705 (2021).

[93] M. G. Ancona and G. J. Iafrate, Quantum correction to the equation of state of an electron gas in a semiconductor, Phys. Rev. B **39**, 9536 (1989).

[94] D. M. Ceperley, Path integrals in the theory of condensed helium, Rev. Mod. Phys. **67**, 279 (1995).

[95] M. F. Herman, E. J. Bruskin, and B. J. Berne, On path integral Monte Carlo simulations, J. Chem. Phys. **76**, 5150 (1982).

[96] M. Takahashi and M. Imada, Monte Carlo calculation of quantum systems, J. Phys. Soc. Jpn. **53**, 963 (1984).

[97] N. Metropolis, A. W. Rosenbluth, M. N. Rosenbluth, A. H. Teller, and E. Teller, Equation of state calculations by fast computing machines, J. Chem. Phys. **21**, 1087 (1953).

[98] M. Boninsegni, N. V. Prokofev, and B. V. Svistunov, Worm algorithm and diagrammatic Monte Carlo: A new approach to continuous-space path integral Monte Carlo simulations, Phys. Rev. E **74**, 036701 (2006).

[99] E. Y. Loh, J. E. Gubernatis, R. T. Scalettar, S. R. White, D. J. Scalapino, and R. L. Sugar, Sign problem in the numerical simulation of many-electron systems, Phys. Rev. B **41**, 9301 (1990).

[100] M. Troyer and U. J. Wiese, Computational Complexity and Fundamental Limitations to Fermionic Quantum Monte Carlo Simulations, Phys. Rev. Lett. **94**, 170201 (2005).

[101] T. Dornheim, Fermion sign problem in path integral Monte Carlo simulations: Quantum dots, ultracold atoms, and warm dense matter, Phys. Rev. E **100**, 023307 (2019).

[102] T. Dornheim, Fermion sign problem in path integral Monte Carlo simulations: Grand-canonical ensemble, J. Phys. A: Math. Theor. **54**, 335001 (2021).

[103] D. M. Ceperley, Fermion nodes, J. Stat. Phys. **63**, 1237 (1991).

[104] K. P. Driver and B. Militzer, All-Electron Path Integral Monte Carlo Simulations of Warm Dense Matter: Application to Water and Carbon Plasmas, Phys. Rev. Lett. **108**, 115502 (2012).

[105] B. Militzer and K. P. Driver, Development of Path Integral Monte Carlo Simulations with Localized Nodal Surfaces for Second-Row Elements, Phys. Rev. Lett. **115**, 176403 (2015).

[106] K. P. Driver, F. Soubiran, and B. Militzer, Path integral Monte Carlo simulations of warm dense aluminum, Phys. Rev. E **97**, 063207 (2018).

[107] M. Boninsegni, Nikolay Prokof'ev, and B. Svistunov, Worm Algorithm for Continuous-Space Path Integral Monte Carlo Simulations, Phys. Rev. Lett. **96**, 070601 (2006).

[108] J. Hofmann, M. Barth, and W. Zwerger, Short-distance properties of coulomb systems, Phys. Rev. B **87**, 235125 (2013).

[109] H. Yasuhara and Y. Kawazoe, A note on the momentum distribution function for an electron gas, Physica A **85**, 416 (1976).

[110] A. K. Rajagopal, J. C. Kimball, and M. Banerjee, Short-ranged correlations and the ferromagnetic electron gas, Phys. Rev. B **18**, 2339 (1978).

[111] T. Dornheim, S. Groth, A. V. Filinov, and M. Bonitz, Path integral Monte Carlo simulation of degenerate electrons: Permutation-cycle properties, J. Chem. Phys. **151**, 014108 (2019).

[112] B. Farid, V. Heine, G. E. Engel, and I. J. Robertson, Extremal properties of the Harris-Foulkes functional and an improved screening calculation for the electron gas, Phys. Rev. B **48**, 11602 (1993).

[113] A. Holas, Exact asymptotic expression for the static dielectric function of a uniform electron liquid at large wave vector, in *Strongly Coupled Plasma Physics*, edited by F.J. Rogers and H.E. DeWitt (Plenum, New York, 1987).

[114] S. Chiesa, D. M. Ceperley, R. M. Martin, and M. Holzmann, Finite-Size Error in Many-Body Simulations with Long-Range Interactions, Phys. Rev. Lett. **97**, 076404 (2006).

[115] T. Dornheim and J. Vorberger, Overcoming finite-size effects in electronic structure simulations at extreme conditions, J. Chem. Phys. **154**, 144103 (2021).

[116] M. Holzmann, R. C. Clay, M. A. Morales, N. M. Tubman, D. M. Ceperley, and C. Pierleoni, Theory of finite size effects for electronic quantum Monte Carlo calculations of liquids and solids, Phys. Rev. B **94**, 035126 (2016).

[117] P. Sperling, E. J. Gamboa, H. J. Lee, H. K. Chung, E. Galtier, Y. Omarbakiyeva, H. Reinholz, G. Röpke, U. Zastrau, J. Hastings, L. B. Fletcher, and S. H. Glenzer, Free-Electron

X-Ray Laser Measurements of Collisional-Damped Plasmons in Isochorically Heated Warm Dense Matter, Phys. Rev. Lett. **115**, 115001 (2015).

[118] K. Ramakrishna, A. Cangi, T. Dornheim, A. Baczewski, and J. Vorberger, First-principles modeling of plasmons in aluminum under ambient and extreme conditions, Phys. Rev. B **103**, 125118 (2021).

[119] C. Mo, Z. Fu, W. Kang, P. Zhang, and X. T. He, First-Principles Estimation of Electronic Temperature from X-Ray Thomson Scattering Spectrum of Isochorically Heated Warm Dense Matter, Phys. Rev. Lett. **120**, 205002 (2018).

[120] C. Lin, F. H. Zong, and D. M. Ceperley, Twist-averaged boundary conditions in continuum quantum Monte Carlo algorithms, Phys. Rev. E **64**, 016702 (2001).

[121] G. G. Spink, R. J. Needs, and N. D. Drummond, Quantum Monte Carlo study of the three-dimensional spin-polarized homogeneous electron gas, Phys. Rev. B **88**, 085121 (2013).

[122] M. Holzmann, B. Bernu, C. Pierleoni, J. McMinis, D. M. Ceperley, V. Olevano, and L. Delle Site, Momentum Distribution of the Homogeneous Electron Gas, Phys. Rev. Lett. **107**, 110402 (2011).

[123] S. H. Glenzer and R. Redmer, X-ray Thomson scattering in high energy density plasmas, Rev. Mod. Phys. **81**, 1625 (2009).

[124] See Supplemental Material at http://link.aps.org/supplemental/10.1103/PhysRevE.104.055206 for all PIMC results for the momentum distribution presented in this work.